Title	Periportal macrophages protect against commensal-driven liver inflammation
Author(s)	Miyamoto, Yu; Kikuta, Junichi; Matsui, Takahiro et al.
Citation	Nature. 2024, 629, p. 901-909
Version Type	AM
URL	https://hdl.handle.net/11094/95817
rights	
Note	

Title

Periportal macrophages protect against commensal-driven liver inflammation

Authors

Yu Miyamoto[1,2,3], Junichi Kikuta[1,2,3,4], Takahiro Matsui[1,5], Tetsuo Hasegawa[1], Kentaro Fujii[1,2,3],

Daisuke Okuzaki[2,6], Yu-chen Liu[2,6], Takuya Yoshioka[7], Shigeto Seno[8], Daisuke Motooka[2,6],

Yutaka Uchida[1,2,3,4], Erika Yamashita[1,2,3], Shogo Kobayashi[9], Hidetoshi Eguchi[9], Eiichi Morii[5],

Karl Tryggvason[10], Takashi Shichita[11], Hisako Kayama[2,12], Koji Atarashi[13], Jun Kunisawa[7],

Kenya Honda[13], Kiyoshi Takeda[2,12], and Masaru Ishii[1,2,3,4*]

Affiliations

[1]Department of Immunology and Cell Biology, Graduate School of Medicine and Frontier

Biosciences, Osaka University, Osaka, Japan

[2]WPI-Immunology Frontier Research Center, Osaka University, Osaka, Japan

[3]Life-omics Research Division, Institute for Open and Transdisciplinary Research Initiative,

Osaka University, Osaka, Japan

[4]Laboratory of Bioimaging and Drug Discovery, National Institutes of Biomedical Innovation,

Health and Nutrition, Osaka, Japan

[5]Department of Pathology, Graduate School of Medicine, Osaka University, Osaka, Japan

[6]Genome Information Research Center, Research Institute for Microbial Diseases, Osaka University, Osaka, Japan

[7]Laboratory of Vaccine Materials, Center for Vaccine and Adjuvant Research, National Institutes of Biomedical Innovation, Health and Nutrition, Osaka, Japan

[8]Department of Bioinformatic Engineering, Graduate School of Information Science and Technology, Osaka University, Osaka, Japan

[9]Department of Gastroenterological Surgery, Graduate School of Medicine, Osaka University, Osaka, Japan

[10]Cardiovascular & Metabolic Disorders Program, Duke-NUS, Duke-NUS Medical School, Singapore, Singapore

[11]Laboratory for Neuroinflammation and Repair, Medical Research Institute, Tokyo Medical and Dental University, Tokyo, Japan

[12]Department of Microbiology and Immunology, Graduate School of Medicine, Osaka University, Osaka, Japan

[13]Department of Microbiology and Immunology, School of Medicine, Keio University, Tokyo, Japan

*Corresponding Author:

Masaru Ishii, Department of Immunology and Cell Biology, Graduate School of Medicine and

Frontier Biosciences, Osaka University, 2-2 Yamada-oka, Suita, Osaka 565-0871, Japan

Tel: +81-6-6879-3880, Fax: +81-6-6879-3889, E-mail: mishii@icb.med.osaka-u.ac.jp

Abstract

The liver is the main gateway from the gut, and the unidirectional sinusoidal flow from portal to central veins constitutes heterogenous zones, including the periportal vein (PV) and pericentral vein zones[1–5]; however, functional differences in the immune system in each zone remain poorly understood. Here, intravital imaging revealed that inflammatory responses were suppressed in PV zones. The zone-specific single-cell transcriptomics detected an immunosuppressive macrophage subset enriched in PV zones that highly expresses IL-10 and Marco, a scavenger receptor sequestering pro-inflammatory PAMPs/DAMPs, and consequently suppressing immune responses. Induction of the Marco[+] immunosuppressive macrophages depended on gut microbiota, and especially, a specific bacterial family, Odoribacteraceae, was identified to induce this macrophage subset via its postbiotic, isoallo-lithocholic acid. Intestinal barrier leakage results in inflammation in PV zones, which was markedly augmented by Marco-deficient conditions. Chronic liver inflammatory diseases such as primary sclerosing cholangitis (PSC) and non-alcoholic steatohepatitis (NASH) showed decreased Marco[+] macrophages. Functional ablation of Marco[+] macrophages led to PSC-like inflammatory phenotypes related to colitis and exacerbated steatosis in NASH in animal experimental models. Collectively, commensal bacteria induce Marco[+] immunosuppressive macrophages, consequently limiting excessive inflammation at the gateway. Failure of this self-limiting

system promotes hepatic inflammatory disorders such as PSC and NASH.

Main text

The mammalian liver comprises repetitive hexagonal units called lobules in which blood flows unidirectionally from portal veins and hepatic arteries towards draining central veins. This polarised blood flow creates concentration gradients along the portal-central axis for blood substances, such as nutrients and oxygen, as well as physiologically active substances[1,2]. Based on this polarised liver structure, several reports have demonstrated the polarised functions of the periportal vein (PV) and pericentral vein (CV) zones. For example, hepatocytes in PV zones contribute to gluconeogenesis and cholesterol biosynthesis, whereas those in CV zones are involved in glutamine and bile acid production[3–5]. Liver sinusoidal endothelial cells (LSECs) produce different chemokines depending on their zonal location, which may guide the positioning of each immune cell type in the tissue[6,7]. In addition, hepatic stellate cells (HSCs) and LSECs in CV zones are prone to pathological changes upon exposure to carbon tetrachloride, thereby exhibiting overproduction of pathogenic collagens compared to those in PV zones[7,8]. The hepatic immune system consists of an asymmetric distribution of resident immune cells, especially Kupffer cells (resident macrophages), with a greater density around the portal veins[6,9], effectively preventing gut bacteria from entering the systemic circulation[6]. Nevertheless, the spatial heterogeneity in hepatic immune functions has not yet been explored.

In this study, we first performed spatial transcriptomic analysis of murine liver specimens, focusing on the immune/inflammatory system. We could distinguish between PV and CV zones

20 based on the specific expression of *Cyp2f2* and *Cyp2e1*, well-defined zonation markers for

21 hepatocytes in PV and CV zones, respectively[10] (**Fig. 1a**), enabling the extraction of

22 differentially expressed genes in each zone. We then performed the Gene Ontology analysis

23 and selected immunity-related terms for detailed analysis. Periportally enriched immune

24 pathways included many processes involved in the negative regulation of the immune system

25 (**Fig. 1b**). This result suggested that immune/inflammatory responses are more repressed in PV

26 than in CV zones. To directly visualise immune responses in PV and CV zones respectively,

27 we used high-resolution intravital two-photon microscopy to assess the in situ behaviours of

28 locally activated inflammatory cells highly expressing lysozyme M-GFP (LysM-GFP), mainly

29 including neutrophils in the liver, using a laser damage-induced sterile inflammation model.

30 These experiments revealed that neutrophils preferentially accumulated at damage sites in CV

31 zones compared with those in PV zones (**Fig. 1c (top), 1d (left), Supplementary Video 1**).

32 Even in the steady-state liver, neutrophils were inclined to reside in CV zones than in PV zones

33 (**Extended Data Fig. 1, Supplementary Video 2**). Subsequently, we focused on the possible

34 role of resident macrophages in the spatial heterogeneity of inflammatory responses in PV/CV

35 zones. We intravenously administered clodronate liposomes (CLL) which specifically depleted

36 the resident macrophages but not the other phagocytic myeloid cells (**Supplementary Fig. 1a,**

37 **b**). We confirmed that CLL treatment did not alter the expression of most chemokines involved

38 in neutrophil recruitment and did not increase the neutrophil infiltration (**Supplementary Fig.**

7

39 **1b, c**). Once resident macrophages were depleted by CLL (in the resident mac-depleted group),

40 neutrophils were shown to be accumulated equally at damage sites in both PV and CV zones

41 (**Fig. 1c (bottom), 1d (right), Supplementary Video 3**). We also examined the in situ

42 behaviours of CX_3CR1-positive circulating monocytes/macrophages upon the laser-induced

43 tissue damages[11]. We found their skewed accumulation in CV zones, similar to the case with

44 neutrophils (**Extended Data Fig. 2a-c**), which was cancelled by depleting resident

45 macrophages with CLL treatment (**Extended Data Fig. 2d,e**). These results suggest that

46 periportal resident macrophages suppress inflammatory responses, with a greater inhibitory

47 activity in PV zones.

48   To identify the immunosuppressive macrophage subset residing in PV zones, we developed

49 a novel method for collecting liver-resident immune cells based on their locational information

50 (*i.e.*, in PV or CV zones) using transgenic mice globally expressing photoactivatable-GFP (PA-

51 GFP) (**Fig. 1e, Supplementary Fig. 2a**). After in vivo staining with a phycoerythrin (PE)-

52 conjugated anti-E-cadherin antibody to demarcate PV zones[6], the livers were excised and

53 freshly sectioned, followed by photoactivation in either the PV or CV zones using violet laser

54 under microscopic guidance. Photoactivated (GFP^+) $CD45^+$ immune cells were collected for

55 single-cell RNA sequencing, which provided single-cell transcriptomic data for 1,282 cells

56 from PV zones and 1,179 cells from CV zones, including all immune cell types in the murine

57 liver[9,12] (**Fig. 1f, Supplementary Fig. 2b, c**). Kupffer cells (liver resident macrophages) are

58   characterised by the expression of *Adgre1* and *Clec4f* (coding F4/80 and CLEC4F,

59   respectively)[13] (**Supplementary Fig. 2c, d**). Among the different immune cell types in the liver,

60   Kupffer cells can be further divided into at least two subpopulations based on their expression

61   patterns, tentatively termed 'MP1' and 'MP2'. *Marco*, a class A scavenger receptor, was found

62   to be exclusively expressed in the MP2 population (**Fig. 1g, Supplementary Fig. 3**).

63   Additionally, typical anti-inflammatory cytokines, such as *Il10*, *Il1rn*, and *Tgfb1* were shown

64   to be elevated in MP2, indicating the immunosuppressive property of MP2 (**Fig. 1h**). To

65   investigate the spatial distributions of MP1/MP2 in each zone, we calculated a localisation

66   score defined as the ratio of the number of PV zone-derived cells to that of CV zone-derived

67   cells of a given subset: > 1 and < 1 indicate bias towards PV and CV zones, respectively (**Fig.**

68   **1f**). MP2 cells were substantially biased towards PV zones, whereas MP1 cells were biased

69   towards CV zones. Immunofluorescence staining ensured that Marco$^+$ F4/80$^+$ cells (MP2) were

70   exclusively concentrated in E-cadherin$^+$ PV zones; however, Marco$^-$ F4/80$^+$ cells (MP1) were

71   equally scattered across the tissue (**Fig. 1i**). Additionally, we could validate the polarised

72   distribution of neutrophils in CV zones observed using histological analyses (**Extended Data**

73   **Fig. 1**) and confirmed the previous results representing periportal distribution of natural killer

74   T cells (NKT), CX$_3$CR1-expressing macrophages and T cells[6,14]. The spatial transcriptomic

75   analysis also verified periportally polarised expression of the anti-inflammatory molecules,

76   *Il10*, *Il1rn*, and *Tgfb1*, which should be expressed in MP2 (**Supplementary Fig. 2e**).

77   Reanalyses of public murine datasets from the liver cell atlas[9] (large-scale single-cell and

78   spatial transcriptomic data) could detect the presence and skewed distribution of Marco$^+$ IL10$^+$

79   MP2 population (**Extended Data Fig. 3a-d**). Furthermore, based on the reanalyses of public

80   human single-cell transcriptomic database[15], *MARCO-* and *IL10*-expressing macrophage

81   subset could also be detected in the human liver, which should correspond to human MP2

82   (**Extended Data Fig. 3e, f**). This human MP2-like population was shown to be significantly

83   reduced in pathological conditions such as liver cirrhosis[15] (**Extended Data Fig. 3g**). The

84   presence of human MP2 would be further supported by a previous report describing periportal

85   MARCO$^+$ 'non-inflammatory' macrophages in the human liver[16]. These reanalyses of public

86   databases demonstrate that Marco$^+$ immunosuppressive macrophages are commonly present in

87   peri-portal vein regions in mice and humans.

88   Next, we examined the molecular mechanisms underlying the immunosuppressive action

89   of MP2 by focusing on interleukin-10 (IL-10) and Marco. Comparative quantification of *Il10*

90   expression in all the immune and non-immune cell types revealed that MP2 was the major IL-

91   10 producer in the liver (**Fig. 2a, b**). We validated the increased transcriptional activity of *Il10*

92   in MP2 compared to that in MP1 using *Il10*-Venus reporter mice (**Extended Data Fig. 4a**). To

93   examine whether IL-10 signalling affects immune responses in PV zones, we treated mice with

94   an anti-IL-10R blocking antibody and performed intravital imaging to observe neutrophil

95   behaviours upon the laser-induced tissue damages. Neutrophil accumulation at damage sites in

96 PV zones was significantly increased by IL-10 signalling blockade (**Fig. 2c, Supplementary**

97 **Video 4**), indicating that IL-10 from MP2 is crucial for limiting inflammatory responses in PV

98 zones. To investigate the molecular mechanism by which IL-10 regulates neutrophil behaviours,

99 we investigated its effects on the liver-resident cells, particularly in liver sinusoidal endothelial

100 cells (LSECs) and Kupffer cells. We first investigated the spatial expression of the adhesion

101 molecule ICAM-1, the ligand of α_M integrin (Mac1 or CD11b), which has reportedly been

102 crucial for neutrophil adhesion to the liver[17]. We classified LSECs based on CD117 expression:

103 CD117-positive and CD117-negative indicate peri-central venous and peri-portal LSECs,

104 respectively[6], and revealed that ICAM-1 expression was significantly higher in CD117$^+$

105 LSECs than that in CD117$^-$ LSECs (**Extended Data Fig. 5a-c**). Next, we examined whether

106 administering anti-IL-10R antibodies could increase ICAM-1 expression on the periportal

107 CD117$^-$ LSECs, and found that ICAM-1 expression increased in peri-portal LSECs (**Extended**

108 **Data Fig. 5d**). These results suggest that IL-10 locally produced by MP2 suppresses ICAM-1

109 expression on LSECs, thereby inhibiting neutrophil adhesion to the PV zones. Furthermore,

110 we found that blockade of IL-10 signalling elevated the expression level of chemokines, *Cxcl1*

111 and *Cxcl2* in Kupffer cells and periportal LSECs, respectively (**Extended Data Fig. 5e**). These

112 chemokines activate the "inside-out" signalling of integrins in neutrophils, which rapidly

113 changes the integrin structure from the bent form to the upright form, and enhances its binding

114 affinity to the ligands[18]. We also confirmed an increase in staining intensity of α_M integrin on

11

115   neutrophil using fluorescein isothiocyanate (FITC)-conjugated antibodies when blocking IL-

116   10 signalling (**Extended Data Fig. 5f, g**). Additionally, we observed that blockade of IL-10R

117   increased the number of resident Kupffer cells expressing TIM-4, which is known as a marker

118   for endogenous Kupffer cells differentiated from embryonic stem cell progenitors[19], but their

119   polarised distribution was retained (**Supplementary Fig. 4**). The increased density of Kupffer

120   cells with elevated chemokine expressions may synergistically promote neutrophil adhesion to

121   LSECs. Therefore, IL-10 locally secreted from MP2 may act on LSECs and Kupffer cells in

122   periportal regions, suppressing neutrophil adhesion in the two distinct manners. However,

123   administering anti-IL-10R antibodies itself did not affect the number of infiltrating neutrophils

124   in the liver (**Extended Data Fig. 5h**).

125   Flow cytometrical analysis detected a positive correlation between Marco expression and

126   *Il10* transcriptional activity in Kupffer cells (**Extended Data Fig. 4b**), suggesting the

127   functional role of Marco for immunosuppressive (IL-10 producing) activity. Next, we

128   evaluated *Il10* mRNA expression in wild-type (*Marco$^{+/+}$*) and *Marco* knockout (*Marco$^{-/-}$*)

129   Kupffer cells and found that *Il10* expression was significantly decreased under *Marco*-deficient

130   conditions (**Extended Data Fig. 4c**). This result suggests that signalling downstream of Marco

131   stimulates the production of anti-inflammatory cytokines, such as IL-10. Intravital imaging

132   using the laser-induced damage model also verified that *Marco* knockout animals exhibited

133   enhanced inflammatory responses to the damages in PV zones due to the lack of IL-10 signals

12

134 (**Fig. 2d, Extended Data Fig. 4c, Supplementary Video 5**), suggesting a critical function for

135 the Marco-IL-10 axis for exerting the anti-inflammatory effects of MP2.

136   Marco is known as a scavenger receptor for damage-associated molecular patterns

137 (DAMPs) and a broad range of polyanionic substances released from bacteria[20–22]. Since the

138 expression level of Marco in MP2 is significantly higher than those of other pattern recognition

139 receptors, such as TLR2 and TLR4, in periportally residing cells (**Supplementary Fig. 5**), we

140 hypothesised that Marco may also directly contribute to the immunosuppressive phenotype in

141 PV zones by sequestrating these immunostimulatory factors[20,23,24]. To address this issue, we

142 visualised the pathogen-capturing activity of Marco$^+$ and Marco$^-$ Kupffer cells in vitro and in

143 vivo, and demonstrated that Marco$^+$ Kupffer cells preferentially captured fluorescently labelled

144 bacteria (**Extended Data Fig. 6**), suggesting that Marco$^+$ MP2 Kupffer cells exert an anti-

145 inflammatory effect via Marco-dependent sequestration of immunogenic pathogens, in

146 addition to producing abundant anti-inflammatory cytokines, such as IL-10.

147   The liver is directly connected to the gut via the portal vein. Gut commensal microbes or

148 their components, such as lipopolysaccharide (LPS) or metabolites, can easily flow into the

149 liver through the portal vein[25]. Next, we examined the effect of gut commensals on the

150 generation and function of MP2 Kupffer cells. We quantified the MP2 subset in specific

151 pathogen-free (SPF), germ-free (GF), and antibiotic-treated (ABX) mice. To analyse the

152 contribution of pathogen-associated molecular patterns (PAMPs), we compared the findings

13

153   with those from MyD88 knockout mice (MyD88$^{-/-}$) lacking a critical downstream adaptor

154   protein of PAMP receptors. The absolute numbers of sinusoidal F4/80$^+$ macrophages (Kupffer

155   cells) were almost the same under all conditions, irrespective of their location within a lobule.

156   However, the percentages of Marco$^+$ MP2 in GF, ABX, and MyD88$^{-/-}$ mice were significantly

157   decreased compared to those in SPF controls (**Fig. 3a, b, c**). With a decrease in MP2, both

158   Kupffer cells and tissue lysates exhibited reduced *Il10* expression under gut commensal

159   bacteria-depleted conditions compared to SPF controls (**Fig. 3d, e**). To examine whether the

160   decrease in MP2 by depleting gut commensal microbes affects inflammatory responses in PV

161   zones, we performed intravital imaging using antibiotic-treated mice to detect local

162   inflammatory responses upon the laser-induced damages. Neutrophil accumulation in PV zones

163   was significantly enhanced by gut commensal depletion (**Fig. 3f, Supplementary Video 6**),

164   suggesting the critical role of commensal microbe-induced MP2 in the immunosuppressive

165   activity within PV zones.

166   Coincidentally, we found that MP2 numbers varied between mice under different housing

167   conditions (SPF-A and SPF-B mice). A larger population of MP2 was observed in SPF-A (**Fig.**

168   **4a**). We then performed 16S ribosomal RNA (rRNA)-sequencing analysis using the colorectal

169   contents and identified five bacterial candidates that might induce MP2 (**Extended Data Fig.**

170   **7a-c**). Based on the positive correlation between the relative abundance of bacteria and the

171   percentage of Marco$^+$ MP2, we focused on a bacterial family, Odoribacteraceae, which belongs

14

172   to the order Bacteroidales and has recently been shown to be involved in the longevity of

173   "centenarians"[26] **(Fig. 4b, c)**. To determine whether Odoribacteraceae contributes to MP2

174   induction, we inoculated an Odoribacteraceae strain (Odori) or a *Bacteroides stercoris* strain

175   (Stercoris) as the negative control into germ-free mice. In parallel, we transplanted Odori or

176   Stercoris into antibiotic-treated mice and kept the mice with SPF mice in the same cage.

177   Although neither Stercoris nor Odori alone significantly induced MP2 (**Fig. 4d**), MP2

178   induction was augmented under symbiosis of Odori and other commensals (**Fig. 4e**). These

179   results indicated that Odoribacteraceae is critical but not sufficient for inducing MP2.

180   Odoribacteraceae is reportedly associated with bile acid metabolism in the gut lumen and

181   contributes to the production of isoallo-lithocholic acid (isoallo-LCA) from chenodeoxycholic

182   acid-derived metabolites, such as 3-oxoallo-LCA and Δ4-isoLCA, which are supplied by other

183   commensals[26,27]. We measured isoallo-LCA contents in the faeces under the conditions of GF,

184   gnotobiote with Odori alone, and SPF with/without Odori and confirmed that concentration of

185   isoallo-LCA was more than 10-fold higher in the SPF condition with Odori compared with that

186   in other conditions (**Fig. 4f**). This suggests that the symbiosis of Odori and other bacteria is

187   necessary for a sufficient supply of isoallo-LCA. Finally, we examined whether oral

188   administration of isoallo-LCA enhanced MP2 induction and revealed that isoallo-LCA

189   significantly stimulates the induction of Marco$^+$ Kupffer cells and increases the expression

190   levels of *Il10* mRNA (**Fig. 4g, h**), suggesting that the effect of Odoribacteraceae on MP2

191   induction is partly mediated by the postbiotic activity such as producing isoallo-LCA.

192   Regarding the physiological significance of the preferential distribution of MP2 in PV

193   zones, a plausible hypothesis is that specific amounts of gut commensals or their related

194   DAMPs/PAMPs can constitutively reach the liver via the portal vein[25], and MP2 may protect

195   against unfavourable inflammatory responses to such pathogens, especially at the entrance of

196   the liver, that is, hepatic periportal regions. This immunomodulatory mechanism would become

197   critical when the intestinal barrier is impaired, causing an increased number of pathogens to be

198   translocated into the liver, as observed in patients with colitis[28], non-alcoholic fatty liver

199   disease[29,30], autoimmune hepatitis[31,32], obesity[33], and diabetes[33]. To verify this hypothesis, we

200   generated a dextran sodium sulphate (DSS)-induced acute colitis model using $Marco^{+/+}$ (wild-

201   type) and $Marco^{-/-}$ (knockout) mice and analysed inflammatory responses in the liver. In this

202   model, 1% DSS was orally administered for 1 week, and the livers were analysed after an

203   additional 4 days of normal water feeding (**Extended Data Fig. 8a**). In the results, Kupffer

204   cells from $Marco^{-/-}$ mice exhibited decreased production of anti-inflammatory cytokines

205   compared with those from wild-type controls (**Extended Data Fig. 8b**), and consistently,

206   intravital imaging revealed substantially higher infiltration of inflammatory neutrophils into

207   the liver in $Marco^{-/-}$ mice on day 11 (**Extended Data Fig. 8c, d, Supplementary Video 7**). In

208   accordance with the occurrence of the inflammation, $Marco^{-/-}$ mice exhibited a significant

209   reduction in body weight (**Extended Data Fig. 8e**). Next, we introduced a mouse model of

210 chronic colitis by repetitive challenges with DSS to analyse the effect of chronic gut

211 inflammation on the liver (**Fig. 5a**), representing a significant increase in inflammatory

212 lymphocytes (T helper 17 cell: Th17) and neutrophils in the liver of *Marco*^{−/−} mice compared

213 to those in wild-type controls (**Fig. 5b, c**). Intravital imaging indicated an accumulation of

214 inflammatory neutrophils near the portal veins in *Marco*^{−/−} mice (**Fig. 5d, Supplementary**

215 **Video 8**). Consistently, serum markers for hepatic damage, including alanine aminotransferase

216 (ALT) and aspartate aminotransferase (AST), were elevated in *Marco*^{−/−} mice (**Fig. 5e**).

217 Furthermore, the expression levels of the fibrosis markers, *Timp1* and *Col1a1*[32], were also

218 increased, leading to type I collagen accumulation in periportal areas in *Marco*^{−/−} mice (**Fig. 5f,**

219 **g**). Such phenotypes in the *Marco*-deficient condition resemble those observed in chronic

220 human inflammatory liver diseases, such as primary sclerosing cholangitis (PSC). Primary

221 sclerosing cholangitis, an intractable disease of unknown origin that is characterised by chronic

222 inflammation around the bile duct and portal vein regions, leads to progressive fibrosis and

223 sclerosis in these areas[34,35]. Notably, PSC is often complicated by inflammatory bowel diseases

224 and has been associated with microbial translocation from the inflamed gut[34,36,37]. Using

225 clinical liver samples of patients with PSC as well as control liver specimens (six PSC and nine

226 normal control samples), we performed immunofluorescence staining to detect Marco[+] and

227 Marco[−] macrophages, demonstrating that the number of periportal Marco[+] macrophages,

228 corresponding to MP2 in the murine liver, was significantly decreased in the PSC livers

229 compared to those in the controls. However, the number of total macrophages was comparable

230 between PSC and control liver specimens (**Fig. 5h, i**). These results may suggest that Marco-

231 expressing macrophages are present in the human liver, which could be associated with chronic

232 inflammatory liver diseases, such as PSC.

233   Next, we examined the possible roles of MP2 Kupffer cells in non-alcoholic fatty liver

234 disease (NAFLD)/non-alcoholic steatohepatitis (NASH), a common and intractable chronic

235 inflammatory disorder in the liver, often complicated with the leaky gut syndrome[29,30]. Based

236 on the reanalysis of the single-cell data from patients with cirrhosis, the MP2 population was

237 reduced in patients with NAFLD compared with the normal controls (**Extended Data Fig. 3g**),

238 implying that MP2 might be involved in the disease progress. To reveal the relationship

239 between MP2 abundance and NAFLD/NASH development, we used a murine NASH/NAFLD

240 model by feeding a methionine-/choline-deficient high-fat (MCDHF) diet to mice for up to 6

241 weeks and harvested the livers in 2-week increments (**Extended Data Fig. 9a**). As a result, the

242 resident Marco$^+$ TIM-4$^+$ MP2 population was significantly declined by 64.5 % in the first 2

243 weeks (**Extended Data Fig. 9b, c**), which was inversely correlated to the occurrence of

244 inflammatory symptoms, such as elevation of serum AST/ALT and neutrophil infiltration

245 (**Extended Data Fig. 9d-i**). The correlation coefficients between MP2 presence and these

246 symptoms were R = −0.82 for AST, R = −0.76 for ALT, and R = −0.59 for neutrophil

247 accumulation, indicating strong negative correlations (**Extended Data Fig. 9e, g, i**). These

248   results suggest that the severity of the disease activity depends on the paucity level of MP2. We

249   then fed MCDHF diet to $Marco^{-/-}$ (knockout) mice lacking the anti-inflammatory functions of

250   MP2 and detected a more severe liver inflammation (**Extended Data Fig. 9j**) and deteriorated

251   liver histopathology representing a more severe steatosis around the portal veins (**Extended**

252   **Data Fig. 9k. l**). The low value of AST/ALT ratio in $Marco^{-/-}$ mice implies the stress-induced

253   damages in PV zones or more advanced fatty liver disease in $Marco^{-/-}$ mice (**Extended Data**

254   **Fig. 9m**). We also verified that Marco$^+$ MP2 was significantly decreased in human

255   NAFLD/NASH patients (seven samples) compared to the normal controls (nine samples)

256   (**Extended Data Fig. 9n-p**). The pathohistological samples can be classified based on the

257   severity of NAFLD/NASH groups according to the 'Matteoni scoring system'[38], and we could

258   demonstrate that the number of MP2 was remarkably decreased in NASH (more severe) group,

259   compared to those in NAFLD (less severe) group (**Extended Data Fig. 9p**). These results may

260   suggest that Marco-expressing macrophages could be associated with the progression of

261   chronic inflammatory liver diseases, such as NAFLD/NASH as well as PSC.

262   The spatial heterogeneity of constituent cells is critical for tissue integrity. By combining

263   in vivo spatiotemporal imaging and single-cell transcriptomic analyses, we demonstrated the

264   heterogenous immune responsiveness in specific liver segments and newly identified an

265   immunosuppressive Marco-expressing resident macrophage (Kupffer cell) subset, designated

266   as MP2, which preferentially localises in PV zones. The presence of PV-polarised Marco$^+$

267   immunosuppressive Kupffer cells are further supported by previous studies showing higher

268   phagocytic function of periportal Kupffer cells[39] and IL-10 production in response to PAMPs

269   stimulation[40]. Scavenging exogenous toxins, including bacteria, PAMPs, and DAMPs, have

270   been demonstrated to serve as a firewall in the body[41,42]; the concept is well consistent with the

271   function of Marco demonstrated in this study. In 2021, Bleriot *et al*. and Simone *et al*. proposed

272   subsets of Kupffer cell, KC1 and KC2[43,44]. KC2 was regarded as a minor population expressing

273   CD206 and ESAM as markers for this specific population and involved in regulating oxidative

274   stress under fatty liver conditions[43] and activation of $CD8^+$ cytotoxic T cells during hepatitis B

275   virus infection[44]. Nevertheless, regarding the KC2, an immunosuppressive phenotype or

276   polarised distribution towards PV zones has not been reported, and we concluded that

277   KC1/KC2 is a conceptually different classification from MP1/MP2 in this study. Nevertheless,

278   based on the cell markers, we also checked that the $Marco^+$ MP2 subset does not belong to

279   KC2 but instead belongs to KC1 (**Extended Data Fig. 10a-c**). Therefore, MP2 can be redefined

280   as a subset of KC1 and be referred to as "$Marco^+$ KC1" (**Extended Data Fig. 10d**).

281   Developmental origin provides an important clue for understanding macrophage

282   characteristics. Macrophages in the adult body are supplied via two pathways: primitive

283   macrophages are obtained from erythro-myeloid progenitors (EMPs) in the yolk sac, and

284   during later development, additional macrophages are supplied by hematopoietic stem cells in

285   the bone marrow[45,46]. Macrophages from different origins exhibit different cellular properties

286   and functions. For example, yolk sac-derived macrophages have higher self-renewal[45,46] and

287   immunoregulatory[47,48] properties than bone marrow-derived macrophages. To examine the

288   origin of MP1 and MP2 in the liver, we performed parabiosis experiments using CX_3CR1-

289   tdTomato and wild-type parabionts and revealed that both MP1 and MP2 were hardly replaced

290   by the bone marrow-derived circulating populations for up to 20 weeks. Looking into the small

291   number of replaced tdTomato$^+$ macrophages in wild-type parabionts, more than 90 % of these

292   were Marco-negative (**Extended Data Fig. 11a-c**). Also, the bone marrow-derived

293   macrophages did not express TIM-4, a yolk sac-derived resident macrophage

294   marker[19](**Extended Data Fig. 11d**). These results suggest that MP2 is essentially derived from

295   EMPs with high self-renewing capacity and rarely differentiated from hematopoietic stem cells

296   in the bone marrow during the postnatal development. We next deleted the liver resident

297   macrophages with CLL to verify this perspective and analysed the regenerated Kupffer cells

298   after 6 weeks (**Extended Data Fig. 11e-j**). We classified the macrophages using the resident

299   macrophage marker TIM-4 and found that the CLL-treated liver contained survived resident

300   (TIM-4-positive) and bone marrow-derived (TIM-4-negative) populations (**Extended Data**

301   **Fig. 11f-h**). TIM-4$^+$ resident macrophages showed greater percentage of Marco-expressing

302   cells and higher expression of *Il10* mRNA compared to TIM-4$^-$ bone marrow-derived

303   macrophages (**Extended Data Fig. 11i, j**). Beattie *et al.* also compared yolk sac-derived

304   Kupffer cells with bone marrow-derived ones by ingeniously creating the chimeric mice. They

21

305   demonstrated that the bone marrow-derived Kupffer cells did not express Marco, even when

306   stimulated by LPS[49]. The bulk of these results suggests that MP2 should be supplied from

307   EMPs in the yolk sac. Nevertheless, detailed analyses using fate-mapping system are required

308   to elucidate when and how MP1 and MP2 are generated during the liver development.

309   Commensal bacteria and their related pathogens/metabolites that translocate from the gut

310   to the liver contribute to MP2 development in PV zones, which, in turn, suppresses excessive

311   inflammation at the gateway of bacterial entry and maintains homeostasis in the liver. The

312   mechanisms underlying commensal bacteria-induced generation of MP2 remain to be

313   elucidated. However, pattern recognition receptor stimulation by PAMPs or DAMPs in some

314   subpopulations of liver-resident cells, including macrophages (Kupffer cells) and endothelial

315   cells, appears to be involved. In this study, we demonstrated that a specific family of

316   commensals, Odoribacteraceae, enhanced MP2 induction by supplying a characteristic bile

317   acid metabolite, isoallo-LCA. Isoallo-LCA induces structural changes in the chromatin and

318   facilitates DNA binding of transcription factors, particularly the nuclear hormone receptor

319   NR4A1[27]. In macrophages, NR4A1 plays a critical role in inducing anti-inflammatory

320   properties, such as elevating IL-10 production[50]. Because Kupffer cells also express abundant

321   NR4A1, this molecule may be involved in MP2 differentiation. Additionally, under depleting

322   the gut commensals with antibiotic treatment, oral administration of isoallo-LCA did not induce

323   MP2 (**Extended Data Fig. 7d-f**), suggesting that the interaction of Odoribacteraceae and other

324   bacteria is necessary not only for a sufficient production of isoallo-LCA but also for the

325   induction of MP2 by isoallo-LCA. This is consistent with the present results that

326   Odoribacteraceae could enhance the generation of MP2 when co-existence with other

327   commensals under SPF conditions but could not solely induce MP2 (**Fig. 4d, e**).

328   This study demonstrated the biological significances of the spatially heterogeneous

329   distribution of Kupffer cell subsets with distinct functions. As a gateway from the gut, the liver

330   is inherently vulnerable to external pathogens, and PV zones are prone to inflammation due to

331   biased accumulation of immune cells, especially Kupffer cells[6,9]. The present results led to a

332   novel concept that the immunomodulatory activity of MP2 in liver PV zones is critical for

333   maintaining healthy conditions against gut commensal infection, and disruption of this

334   protective mechanism may be correlated with intractable liver diseases, such as PSC and

335   NASH. Also, our comprehensive analyses with laboratory animals and human samples

336   demonstrated that MP2 could be a promising target for developing therapeutic approaches

337   against these refractory liver diseases.

Main references

339   1.   Jungermann, K. & Kietzmann, T. Zonation of parenchymal and nonparenchymal

340   metabolism in liver. *Annu. Rev. Nutr.* **16**, 179–203 (1996).

341   2.   Mizukami, K. *et al.* In vivo O_2 imaging in hepatic tissues by phosphorescence lifetime

342   imaging microscopy using Ir(III) complexes as intracellular probes. *Sci. Rep.* **10**, 1–14

343   (2020).

344   3.   Nauck, M., Wölfle, D., Katz, N. & Jungermann, K. Modulation of the glucagon-

345   dependent induction of phosphoenolpyruvate carboxykinase and tyrosine

346   aminotransferase by arterial and venous oxygen concentrations in hepatocyte cultures.

347   *Eur. J. Biochem.* **119**, 657–661 (1981).

348   4.   Jungermann, K., Heilbronn, R., Katz, N. & Sasse, D. The glucose/glucose-6-phosphate

349   cycle in the periportal and perivenous zone of rat liver. *Eur. J. Biochem.* **123**, 429–436

350   (1982).

351   5.   Jungermann, K. & Katz, N. Functional specialization of different hepatocyte populations.

352   *Physiol. Rev.* **69**, 708–764 (1989).

353   6.   Gola, A. *et al.* Commensal-driven immune zonation of the liver promotes host defence.

354   *Nature* **589**, 131–136 (2021).

355   7.   Su, T. *et al.* Single-cell transcriptomics reveals zone-specific alterations of liver

356   sinusoidal endothelial cells in cirrhosis. *Cmgh* **11**, 1139–1161 (2021).

357   8.   Dobie, R. *et al.* Single-cell transcriptomics uncovers zonation of function in the

358   mesenchyme during liver fibrosis. *Cell Rep.* **29**, 1832-1847 (2019).

359   9.   Guilliams, M. *et al.* Spatial proteogenomics reveals distinct and evolutionarily

360   conserved hepatic macrophage niches. *Cell* **185**, 379-396 (2022).

361   10.   Halpern, K. B. *et al.* Single-cell spatial reconstruction reveals global division of labour

362   in the mammalian liver. *Nature* **542**, 352–356 (2017).

363   11.   Dal-Secco, D. *et al.* A dynamic spectrum of monocytes arising from the in situ

364   reprogramming of CCR2^{+} monocytes at a site of sterile injury. *J. Exp. Med.* **212**, 447–

365   456 (2015).

366   12.   Remmerie, A. *et al.* Osteopontin expression identifies a subset of recruited macrophages

367   distinct from Kupffer cells in the fatty liver. *Immunity* **53**, 641-657 (2020).

368   13.   Scott, C. L. *et al.* Bone marrow-derived monocytes give rise to self-renewing and fully

369   differentiated Kupffer cells. *Nat. Commun.* **7**, 1–10 (2016).

370   14.   English, K. *et al.* The liver contains distinct interconnected networks of CX3CR1^{+}

371   macrophages, XCR1^{+} type 1 and CD301a^{+} type 2 conventional dendritic cells embedded

372   within portal tracts. *Immunol. Cell Biol.* **100**, 394–408 (2022).

373   15.   Ramachandran, P. *et al.* Resolving the fibrotic niche of human liver cirrhosis at single-

374   cell level. *Nature* **575**, 512-518 (2019).

375   16.   MacParland, S. A. *et al.* Single cell RNA sequencing of human liver reveals distinct

376 intrahepatic macrophage populations. *Nat. Commun.* **9**, 1–21 (2018).

377 17. McDonald, B. *et al.* Intravascular danger signals guide neutrophils to sites of sterile

378 inflammation. *Science* **330**, 362–6 (2010).

379 18. Lefort, C. T. & Ley, K. Neutrophil arrest by LFA-1 activation. *Front. Immunol.* **3**, 1–10

380 (2012).

381 19. Sakai, M. *et al.* Liver-derived signals sequentially reprogram myeloid enhancers to

382 initiate and maintain Kupffer cell identity. *Immunity* **51**, 655-670 (2019).

383 20. Shichita, T. *et al.* MAFB prevents excess inflammation after ischemic stroke by

384 accelerating clearance of damage signals through MSR1. *Nat. Med.* **23**, 723–732 (2017).

385 21. Andersson, L. & Freeman, M. W. Functional changes in scavenger receptor binding

386 conformation are induced by charge mutants spanning the entire collagen domain. *J.*

387 *Biol. Chem.* **273**, 19592–19601 (1998).

388 22. Ojala, J. R. M., Pikkarainen, T., Tuuttila, A., Sandalova, T. & Tryggvason, K. Crystal

389 structure of the cysteine-rich domain of scavenger receptor MARCO reveals the

390 presence of a basic and an acidic cluster that both contribute to ligand recognition. *J.*

391 *Biol. Chem.* **282**, 16654–16666 (2007).

392 23. Mukhopadhyay, S. *et al.* SR-A/MARCO-mediated ligand delivery enhances

393 intracellular TLR and NLR function, but ligand scavenging from cell surface limits

394 TLR4 response to pathogens. *Blood* **117**, 1319–1328 (2011).

395   24.   Jing, J. *et al.* Role of macrophage receptor with collagenous structure in innate immune

396   tolerance. *J. Immunol.* **190**, 6360–6367 (2013).

397   25.   Leinwand, J. C. *et al.* Intrahepatic microbes govern liver immunity by programming

398   NKT cells. *J. Clin. Invest.* **132**, e151725 (2022).

399   26.   Sato, Y. *et al.* Novel bile acid biosynthetic pathways are enriched in the microbiome of

400   centenarians. *Nature* **599**, 458–464 (2021).

401   27.   Li, W. *et al.* A bacterial bile acid metabolite modulates Treg activity through the nuclear

402   hormone receptor NR4A1. *Cell Host Microbe* **29**, 1366-1377 (2021).

403   28.   Spadoni, I. *et al.* A gut-vascular barrier controls the systemic dissemination of bacteria.

404   *Science* **350**, 830–834 (2015).

405   29.   Sookoian, S. *et al.* Intrahepatic bacterial metataxonomic signature in non-alcoholic fatty

406   liver disease. *Gut* **69**, 1483–1491 (2020).

407   30.   Luther, J. *et al.* Hepatic injury in nonalcoholic steatohepatitis contributes to altered

408   intestinal permeability. *Cell. Mol. Gastroenterol. Hepatol.* **1**, 222–232 (2015).

409   31.   Manfredo Vieira, S. *et al.* Translocation of a gut pathobiont drives autoimmunity in mice

410   and humans. *Science* **360**, 1156–1161 (2018).

411   32.   Nakamoto, N. *et al.* Gut pathobionts underlie intestinal barrier dysfunction and liver T

412   helper 17 cell immune response in primary sclerosing cholangitis. *Nat. Microbiol.* **4**,

413   492–503 (2019).

414 33. Thaiss, C. A. *et al.* Hyperglycemia drives intestinal barrier dysfunction and risk for

415   enteric infection. *Science* **359**, 1376–1383 (2018).

416 34. Lazaridis, K. N. & LaRusso, N. F. Primary sclerosing cholangitis. *N. Engl. J. Med.* **375**,

417   1161–1170 (2016).

418 35. Dyson, J. K., Beuers, U., Jones, D. E. J., Lohse, A. W. & Hudson, M. Primary sclerosing

419   cholangitis. *Lancet* **391**, 2547–2559 (2018).

420 36. Horsley-Silva, J. L., Carey, E. J. & Lindor, K. D. Advances in primary sclerosing

421   cholangitis. *Lancet Gastroenterol. Hepatol.* **1**, 68–77 (2016).

422 37. O'Toole, A. *et al.* Primary sclerosing cholangitis and disease distribution in

423   inflammatory bowel disease. *Clin. Gastroenterol. Hepatol.* **10**, 439–441 (2012).

424 38. Matteoni, C. A. *et al.* Nonalcoholic fatty liver disease: A spectrum of clinical and

425   pathological severity. *Gastroenterology* **116**, 1413–1419 (1999).

426 39. Bouwens, L., Baekeland, M., De Zanger, R. & Wisse, E. Quantitation, tissue distribution

427   and proliferation kinetics of Kupffer cells in normal rat liver. *Hepatology* **6**, 718–22

428   (1986).

429 40. Knoll, P. *et al.* Human Kupffer cells secrete IL-10 in response to lipopolysaccharide

430   (LPS) challenge. *J. Hepatol.* **22**, 226–229 (1995).

431 41. Balmer, M. L. *et al.* The liver may act as a firewall mediating mutualism between the

432   host and its gut commensal microbiota. *Sci. Transl. Med.* **6**, 237ra66 (2014).

433   42.   van der Laan, L. J. *et al.* Regulation and functional involvement of macrophage

434   scavenger receptor MARCO in clearance of bacteria in vivo. *J. Immunol.* **162**, 939–47

435   (1999).

436   43.   Blériot, C. *et al.* A subset of Kupffer cells regulates metabolism through the expression

437   of CD36. *Immunity* **54**, 2101-2116 (2021).

438   44.   De Simone, G. *et al.* Identification of a Kupffer cell subset capable of reverting the T

439   cell dysfunction induced by hepatocellular priming. *Immunity* **54**, 2089-2100 (2021).

440   45.   Yona, S. *et al.* Fate mapping reveals origins and dynamics of monocytes and tissue

441   macrophages under homeostasis. *Immunity* **38**, 1073–1079 (2013).

442   46.   Liu, Z. *et al.* Fate mapping via Ms4a3-expression history traces monocyte-derived cells.

443   *Cell* **178**, 1509-1525 (2019).

444   47.   van de Laar, L. *et al.* Yolk sac macrophages, fetal liver, and adult monocytes can

445   colonize an empty niche and develop into functional tissue-resident macrophages.

446   *Immunity* **44**, 755–768 (2016).

447   48.   Tran, S. *et al.* Impaired Kupffer cell self-renewal alters the liver response to lipid

448   overload during non-alcoholic steatohepatitis. *Immunity* **53**, 627-640 (2020).

449   49.   Beattie, L. *et al.* Bone marrow-derived and resident liver macrophages display unique

450   transcriptomic signatures but similar biological functions. *J. Hepatol.* **65**, 758–768

451   (2016).

452 50. Koenis, D. S. *et al.* Nuclear Receptor Nur77 Limits the Macrophage Inflammatory

453   Response through Transcriptional Reprogramming of Mitochondrial Metabolism. *Cell*

454   *Rep.* **24**, 2127-2140 (2018).

455

Figure Legends

457

458 **Fig. 1. A periportal macrophage subset suppressively regulates periportal immune**

459 **activation. a**, Spatial transcriptomics showing hepatic zonation (n = 4): gene expression of

460 *Cyp2f2* (left-upper) and *Cyp2e1* (left-lower), identified zones (right-upper, blue: PV zones,

461 orange: CV zones, green: marginal zones), and H&E staining (right-lower). **b**, Immune

462 pathways enriched in PV zones (vs. CV zones). P-values were determined using one-sided

463 Fisher's exact test. **c**, Representative intravital images of in situ inflammatory responses of

464 neutrophils against sterile laser-induced damages in control (top) and macrophage-depleted

465 mice (bottom) [n = 14 each, green: neutrophils, white: damaged sites (autofluorescence), and

466 blue: collagens visualised using second harmonic generation (SHG)]. Scale bar: 100 μm. **d**,

467 Neutrophil accumulation scores in control (left) and macrophage-depleted mice (right). Data

468 are presented as means ± standard error of the mean (SEM). P-value was determined using

469 paired two-sided Mann–Whitney U test at 3 h. **e**, Schematics of isolation of zone-specifically

470 labelled immune cells. Scale bar: 50 μm. **f**, t-Distributed Stochastic Neighbour Embedding

471 (tSNE) plot depicting each immune cell cluster and location (left). The localisation score

472 (PV/CV ratio) (right). **g**, Expression of *Clec4f* and *Marco* shown on the tSNE plot. **h**, Violin

473 plots depicting expression of the anti-inflammatory cytokines *Il10*, *Il1rn*, *and Tgfb1* in MP1

474 and MP2. Statistical significance was determined using a two-sided Wilcoxon Rank Sum test.

475 **i**, Representative immunofluorescence image showing Marco (green), F4/80 (red), and E-

476 cadherin (blue) (left, n = 4, 33 visual fields). Localisation score (PV/CV ratio) of Marco$^+$ and

477 Marco$^-$ macrophages (right). Scale bar: 100 μm. Data are presented as means (asterisk) with

478 medians, smallest observations, lower and upper quartiles, and largest observations. Statistical

479 significance was determined using unpaired two-sided Mann–Whitney U test. The exact *p*-

480 value is 2.2×10^{-16}.

481

Fig. 2. The Marco–IL-10 axis is necessary for establishing an immunosuppressive niche in periportal regions. a, mRNA expression of *Il10* in MP2 and other immune cell types identified in the single-cell transcriptomics. Statistical significance was determined using a two-sided Wilcoxon Rank Sum test. The *p*-value was adjusted based on Bonferroni correction. **b**, Relative mRNA expression of *Il10* to *Gapdh* in MP2 (n = 6), LSECs (n = 8), HSCs (n = 7), and hepatocytes (n = 6). **c**, Representative intravital images of in situ inflammatory responses of neutrophils upon laser-induced tissue damages under treatment with isotype control antibody (left) and anti-IL-10R antibody (centre) [n = 6 per condition, green: neutrophils, white: damaged sites (autofluorescence), and blue: SHG (tissue collagens)]. Scale bar: 100 μm. Spatially biased neutrophil accumulation at 3 h post-laser ablation is shown as the PV/CV ratio (right). **d**, Representative intravital images of in situ inflammatory responses of neutrophils upon laser-induced tissue damages in *Marco*$^{+/+}$ wild-type (left, n = 10) and *Marco*$^{-/-}$ knockout (centre, n = 7) mice [green: neutrophils, white: damaged sites, and blue: SHG (tissue collagens)]. Scale bar: 100 μm. Spatially biased neutrophil accumulation at 3 h post-laser ablation is shown as the PV/CV ratio (right). All quantitative data are presented as means (asterisk) with medians, smallest observations, lower and upper quartiles, and largest observations. Statistical significance was determined using unpaired two-sided Mann–Whitney U test.

500

Fig. 3. Gut commensal microbes induce the periportal immunosuppressive Kupffer cells.

a, Representative immunofluorescence images showing Marco (green), F4/80 (red), and E-cadherin (blue) in liver sections from specific pathogen-free (SPF, n = 11, 35 visual fields), germ-free (GF, n = 5, 27 visual fields), antibiotic-treated (ABX, n = 9, 26 visual fields), and MyD88 knockout mice (*MyD88$^{-/-}$*, n = 5, 39 visual fields). Scale bar: 100 μm. **b**, Absolute number of F4/80-positive cells (total Kupffer cells) per visual field. **c**, Percentage of Marco$^+$ immunosuppressive Kupffer cells (MP2) to total Kupffer cells quantified using flow cytometry. **d,e**, Relative mRNA expression of *Il10* to *Gapdh* in total Kupffer cell fractions (d) and tissue lysates (e) from SPF control (n = 9) and ABX (n = 7) mice. **f**, Representative intravital images of in situ inflammatory responses of neutrophils upon laser-induced damage in control (left, n = 10) and ABX (centre, n = 12) mice [green: neutrophils, white: damaged sites, and blue: SHG (tissue collagens)]. Scale bar: 100 μm. Spatially biased neutrophil accumulation at 3 h post-laser ablation is shown as the PV/CV ratio (right). All quantitative data are presented as means (asterisk) with medians, smallest observations, lower and upper quartiles, and largest observations. Statistical significance was determined using unpaired two-sided Mann–Whitney U test.

517

Fig. 4. Odoribacteraceae promotes induction of the periportal immunosuppressive Kupffer cells by providing isoallo-lithocholic acids. a, Percentage of Marco[+] immunosuppressive Kupffer cells (MP2) to total Kupffer cells from SPF-A and SPF-B mice. **b**, Relative abundance (%) of Odoribacteraceae in colorectal contents from SPF-A and SPF-B mice. **c**, Correlation between the abundance of Odoribacteraceae and the percentage of MP2. 'R' indicates the correlation coefficient. **d**, Graphical protocol for generating gnotobiotic mice (left). Odori and Stercoris indicate Odoribacteraceae and *B. Stercoris*, respectively. Percentage of MP2 to total Kupffer cells (right). **e**, Graphical protocol for generating symbiotic conditions of target and SPF microbes (left). Sterile PBS-inoculated GF mice were used as a negative control. Percentage of MP2 to total Kupffer cells (right). **f**, Concentration of isoallo-lithocholic acid (isoallo-LCA) in faeces. **g**, Graphical protocol for oral administration of isoallo-LCA or the vehicle control, dimethyl sulfoxide (DMSO) (left). Percentage of MP2 to total Kupffer cells (right). **h**, Fold changes of *Il10* mRNA expression in Kupffer cells. Data were standardized to ensure a control group mean value of '1'. All quantitative data are presented as means (asterisk) with medians, smallest observations, lower and upper quartiles, and largest observations. Statistical significance was determined using unpaired two-sided Mann–Whitney U test.

534

Fig. 5. Periportal immunosuppressive Kupffer cells protect against gut bacteria-driven inflammation. a, Experimental design of chronic colitis-induced liver inflammation. **b**, The heatmap representing fold changes of each immune cell type against the healthy control. **c**, Absolute numbers of CD45-positive cells, neutrophils, and Th17 cells from DSS-treated $Marco^{+/+}$ (n = 12) and $Marco^{-/-}$ (n = 11) mice. **d**, Representative intravital images of infiltrating LysM-GFP$^+$ cells, including neutrophils/macrophages, in DSS-treated $Marco^{+/+}$ and $Marco^{-/-}$ mice on day 39 [n = 3 per condition, green: LysM-GFP$^+$ cells, blue: SHG (tissue collagens)]. Scale bar: 100 μm. PV, portal vein; CV, central vein. **e**, Serum ALT and AST levels from DSS-treated $Marco^{+/+}$ (n = 14) and $Marco^{-/-}$ (n = 16) mice. **f**, Relative mRNA expression of fibrosis markers *Timp1* (left) and *Col1a1* (right) to *Gapdh* in tissue lysates from DSS-treated $Marco^{+/+}$ (n = 12) and $Marco^{-/-}$ (n = 11) mice. **g**, Representative immunofluorescence images are shown (left). Scale bar: 100 μm. Quantification of type I collagen accumulations in PV zones: $Marco^{+/+}$ (n = 6, 12 visual fields) and $Marco^{-/-}$ (n = 7, 14 visual fields). **h,** Representative immunofluorescence images showing MARCO (green), CD68 (red), and CK19 (cyan) in human livers: PSC (n = 6, 18 visual fields) and normal controls (n = 9, 27 visual fields). Scale bar: 100 μm. **i**, Quantified information: the absolute numbers of CD68-positive cells (macrophages) per visual field (left). Percentage of Marco$^+$ cells to total macrophages in visual fields (centre). The exact *p*-value is 1.166×10^{-12}. Percentage of periportal Marco$^+$

553　macrophages within 200 μm from bile ducts (right). The exact p-value is 1.92×10^{-8}. All

554　quantitative data are presented as means (asterisk) with medians, smallest observations, lower

555　quartiles, upper quartiles, and largest observations. Statistical significance was determined

556　using unpaired two-sided Mann–Whitney U test.

557 **Methods**

558 **Mice**

559   C57BL/6 wild-type and germ-free mice were purchased from CLEA Japan, Inc. $Myd88^{-/-}$[51]

560   mice were purchased from Oriental Bio Service, Inc. Photoactivatable-GFP (PA-GFP)[52] mice

561   were provided by Dr. Michel Nussenzweig (Rockefeller University). Rosa-tdTomato (Ai9)[53]

562   and Cx3cr1-Cre[45] mice were purchased from the Jackson Laboratory. Generation of

563     $Marco^{-/-}$[54], $Il10$-Venus[55], LysM-GFP[56], and CX_3CR1-GFP[57] mice has been described

564   previously. This study used 8–20-week-old female or male mice (no sex difference was

565   confirmed). All mice were randomly housed in groups and selected for the experiments. Mice

566   were fed a normal diet (MF diet; Oriental Yeast Co., Ltd.) and maintained at 23 ± 1.5 °C and

567   45 ± 15% relative humidity under a 12 h/12 h light/dark cycle in specific pathogen-free animal

568   facilities at Osaka University. All animal experiments were approved by the Institutional

569   Animal Experimental Committee of Osaka University.

570

571 **Parabiosis**

572 Transgenic mice (Rosa-LSL-tdTomato:Cx3cr1-Cre) were surgically connected to wild-type

573 mice as described previously[58]. Briefly, the lateral skin incisions were made from the elbow to

574 the knee in each mouse, and then the forelimbs and hind limbs were tied together using silk

575 sutures. We made approximately 1 cm incisions in the peritoneum of each mouse, and the mice

576 were attached them using silk sutures. The skin incisions were closed using stainless steel

577 wound clips.

578

579 **Drug treatment**

580 To deplete Kupffer cells, we used clodronate liposome according to a previous study[59]. Briefly,

581 500 µg clodronate liposome (#MKV100, Cosmo Bio) in 200 µL phosphate-buffered saline

582 (PBS) was intravenously injected via the tail vein (**Fig.1**, **Extended Data Fig.2,**

583 **Supplementary Fig. 1**) and 650 µg clodronate liposome in 200 µL PBS was injected in the

584 same way (**Extended Data Fig. 11**). The mice were used for further experiments 2 days later

585 (**Fig.1**, **Extended Data Fig.2, Supplementary Fig. 1**) and 6 weeks later (**Extended Data Fig.**

586 **11**), respectively. To examine the effects of in vivo blockade of IL-10 signalling, we used an

587 anti-IL-10R antibody based on the method of a previous study[60]. Briefly, 200 µg anti-IL-10R

588 antibody (#112710, BioLegend) or rat IgG1,κ antibody (#400432, BioLegend) as isotype

589 control was intraperitoneally injected every 2 days for 5 days, and the mice were used for the

590 experiments on day 5. To assess MP2 induction by isoallo-lithocholic acid (isoallo-LCA)

591 treatment, we administered 200 µg of isoallo-LCA (#29542, Cayman) via oral gavage. Prior to

592 the administration, 10 mg/mL isoallo-LCA in DMSO was prepared as a stock solution and

593 stored at −80 °C before use. From this stock, 1 mg/mL isoallo-LCA solution was prepared by

594 diluting 10 times with PBS, and 200 µL was administered daily for 2 weeks. As a control, 10%

595 (v/v) DMSO in PBS was administered similarly. To deplete the gut commensals, we treated

596 mice with antibiotics, similar to a previous study[61]. Briefly, 8-week-old mice received 1 g/L

597 ampicillin sodium (#19769-64, Nacalai), 0.5 g/L vancomycin hydrochloride (#36137-91,

598 Nacalai), 1 g/L neomycin sulphate (#19767-84, Nacalai), and 1 g/L metronidazole (#23254-64,

599 Nacalai) in their drinking water for 6 weeks (**Fig, 3 and 4**). The antibiotic-containing water

600 was replaced with a fresh one every 4 days. In **Extended Data Fig. 7d-f**, mice received the

601 same antibiotic-containing water for 1 week, following half the concentration of the complete

602 antibiotic-containing water for 2 weeks during the isoallo-LCA treatment.

603

604 **Spatial transcriptome analysis using Visium™**

605   The mice were euthanised via CO_2 overdose. The liver was immediately excised, and each

606 liver lobe was embedded in Tissue-Tek O.C.T. Compound (Sakura) and snap-frozen in

607 isopentane (Sigma) chilled by liquid nitrogen. The frozen tissue blocks were sliced into 10 μm

608 sections and placed within the capture area of a 10× Visium Spatial Gene expression slide (10×

609 Genomics). The 10x Visium cDNA library was prepared according to the manufacturer's

610 instructions. cDNA libraries from four samples were sequenced on a NovaSeq 6000 (Illumina,

611 USA) platform in a 28+120-base paired-end mode.

612   The raw sequenced reads were processed using 10× Genomics CellRanger 1.0.0. The four

613 sample data were merged to account for the batch effect between samples using Scanorama[62]

614 and Scanpy[63]. The expression levels of the hepatic zonation markers *Cyp2f2* and *Cyp2e1*[10] were

615 used to classify the Visium spots into portal vein (PV) and central vein (CV) zones. Briefly, the

616 expression levels of *Cyp2f2* and *Cyp2e1* exhibited a bimodal distribution, and the distributions

617 were fitted for each gene using a 'two-component mixed Gaussian model' (**Supplementary**

618 **Fig. 6**). Establishing a threshold at the junction of the high and low expression distributions

619 should provide a suitable criterion for zonal classification. Visium spots with higher expression

620 of *Cyp2f2* and lower expression of *Cyp2e1* compared with the threshold were defined as PV

621 zones. In contrast, spots with higher expression of *Cyp2e1* and lower expression of *Cyp2f2*

622 compared with the threshold were defined as CV zones. Subsequently, we examined the

623 differentially expressed genes (DEGs) in each zone by statistically comparing the gene

624 expression levels between the identified PV and CV zones with 'Rank genes for characterizing

625 groups' function implemented in Scanpy, and extracted 630 and 340 DEGs, which were

626 enriched in PV and CV zones, respectively. Genes showing adjusted *P*-values (Benjamini-

627 Hochberg method) of more than 0.05 were excluded. We then performed the Gene Ontology

628 analysis using the periportally enriched 630 genes with the software DAVID[64] (version 6.8)

629 and extracted the terms (biological pathways), which contain immune-related genes and show

630 $P < 0.05$.

631

632 **Intravital imaging of the liver and induction of inflammatory immune responses**

633   All surgical procedures in mice were conducted under anaesthesia with isoflurane (#099-

634   06571, Wako). The left lobe of the liver was surgically exposed and gently placed on a cover

635   glass fixed on the imaging stage. The treated mouse was placed in an environmental dark box

636   and warmed to 37°C by an air heater. The internal surface of the liver was observed using an

637   inverted two-photon excitation microscope (A1R-MP, Nikon, Japan) driven by a laser

638   (Chameleon Vision Ti; Sapphire, Coherent) tuned to 870 nm, with a ×20 water immersion

639   objective lens (CFI LWD Lambda S WI, numerical aperture: 0.95, Nikon). Emission

640   wavelengths were detected via bandpass emission filters at 492/SP nm for the second harmonic

641   generation, 525/50 nm for GFP, 575/25 nm for autofluorescence, and 629/56 nm for

642   Qtracker655. This microscopy system was operated using NIS elements software (Nikon).

643   Qtracker655 Vascular Labels (#Q21021MP, Invitrogen) were diluted 20 times in phosphate-

644   buffered saline (PBS) (#14249-95, Nacalai), and 50 µL of the diluted Qtracker655 Vascular

645   Labels was rapidly administered intravenously through a peripheral intravenous line under

646   imaging to detect the PV and CV zones (**Supplementary Video 9**). Image stacks were collected

647   at 3-µm vertical steps up to a depth of 48 µm below the liver surface at an X–Y resolution of

648   512 × 512 pixels (1.24 µm/pixel). Raw imaging data were processed using NIS elements

649   (Nikon) and ImageJ software[65]. Two-dimensional maximum-intensity projection (MIP) images

650   were generated using NIS elements. Background subtraction, median filtering, and binarization

651   were performed using ImageJ. The accumulation score was measured as the integrated area of

42

652   binarized cells within the region of interest. All images and videos are displayed as MIP images.

653   To activate local immune cells, we induced necrotic tissue damages measuring < 20 μm using

654   infrared laser pulses within PV and CV zones, at 10–20 μm away from each blood vessel and

655   below the liver capsule, based on the methods of previous studies with minor modifications[66,67].

656   Intravital imaging commenced immediately after the laser ablation and was performed for 3 h

657   at a time resolution of 30 sec to track the neutrophil movements. Additionally, to observe

658   monocyte/macrophage dynamics, we induced the thermal damages in the liver, and then re-

659   introduced the liver lobe into the mouse body and closed the peritoneum and skin incisions

660   using silk sutures. The mouse was allowed free movement for 24 hours. Monocyte/macrophage

661   accumulation at the damage sites was recorded 24 h post laser ablation (**Extended Data Fig.**

662   **2b**).

663

664   **Zone-specific isolation of leukocytes from the liver**

665   To demarcate the PV zones, we intravenously injected 2 μg of phycoerythrin (PE)-conjugated

666   anti-E-cadherin antibody (#147304, BioLegend) in 200 μL PBS into a PA-GFP mouse. After

667   20 min, the liver was harvested, and fresh tissue sections (250 μm thickness) were cut using a

668   Vibratome (Leica, Germany) in chilled HBSS (#17461-05, Nacalai) containing 25 mM HEPES

669   (#15630080, Gibco) and 2% foetal bovine serum (FBS) (Lot:12B247, Sigma). The sections

670   were placed on glass-bottom dishes (#627860, Greiner) and then covered with absorbent cotton

671 soaked with a cold buffer. The subsequent procedures were performed in the cooled equipment.

672 Photoactivation in PV or CV zones was performed using a single-photon 405 nm violet laser

673 while observing the sections under a two-photon excitation microscope (A1R-MP, Nikon)[52,68].

674 The photoactivated sections were digested in RPMI medium (#61870036, Gibco) containing

675 10 mM HEPES, 0.033 mg/mL Liberase (#5401119001, Roche), 0.05 mg/mL DNase

676 (#LS002139, Worthington), and 0.35 mM $CaCl_2$ (#036-19731, Wako) for 35 min with agitation.

677 The single-cell suspension was filtered through a 100 μm cell strainer, and the undigested

678 material was mashed through a 100 μm cell strainer before centrifugation at 500 × g for 5 min.

679 The supernatant was discarded, and the pellet was resuspended in 100 μL PBS, followed by

680 the addition of 0.2 μL Zombie NIR solution (#423105, BioLegend), and then the samples were

681 incubated for 15 min at room temperature (RT, approximately 25 °C) to stain dead cells. Finally,

682 400 μL autoMACS running buffer (#130-091-221, Miltenyi) was added before fluorescence-

683 activated cell sorting (FACS) staining.

684

685 **Unbiased isolation of leukocytes from the liver**

686 Liver leukocytes were isolated as described previously[15], with slight modifications. Briefly,

687 the livers were minced into smaller pieces using scissors and then digested in RPMI medium

688 containing 0.625 mg/mL collagenase D (#11088858001, Roche), 0.85 mg/mL collagenase V

689 (#C9263, Sigma), 1 mg/mL dispase (#17105041, Gibco), and 30 U/mL DNase (#10104159001,

44

690   Roche) for 20 min with agitation at 37 °C. All the subsequent procedures were conducted at

691   4 °C. The single-cell suspension was filtered through a 100 μm cell strainer, and undigested

692   pieces were mashed through a 100 μm cell strainer before centrifuging at 500 × g for 5 min.

693   The supernatant was discarded, and the pellet was resuspended in 5 mL RPMI containing 2%

694   FBS. The cell suspension was added on 5 mL 33% Percoll (#17089102, GE) in a 15-mL Falcon

695   tube, and centrifuged at 800 × g for 20 min at 20 °C. Next, the top 5.5 mL was aspirated and

696   discarded, and the remainder was washed in additional PBS and centrifuged at 500 × g for 5

697   min. The resulting supernatant was discarded, and the pellet was resuspended in ACK lysis

698   buffer (#A1049201, Gibco) for 3 min to remove red blood cells. The cell suspensions were

699   then washed in PBS containing 2% FBS, filtered through a 70 μm cell strainer, and centrifuged

700   at 500 × g for 5 min. The pellet was resuspended in autoMACS running buffer before FACS

701   staining.

702

703   **Isolation of hepatocytes, liver sinusoidal endothelial cells (LSECs), and hepatic stellate**

704   **cells (HSCs)**

705   Hepatocytes, LSECs, and HSCs were isolated as described previously[69]. Briefly, the livers

706   were perfused with EGTA (#E3889, Sigma) solution and 0.2 mg/mL collagenase A

707   (#10103578001, Roche) solution at a flow rate of 6 mL/min. The livers were mashed through

708   a 100 μm cell strainer and incubated in RPMI medium containing 25 mM HEPES, 0.4 mg/mL

709   collagenase A, and 10 U/mL DNaseI (#10104159001, Roche) for 20 min with agitation at 37°C.

710   After filtration through a 100 μm cell strainer, the cell suspensions were centrifuged at 400 ×

711   g for 7 min and resuspended in ACK lysis buffer for 3 min to remove red blood cells. The cell

712   suspensions were washed in PBS containing 2% FBS and filtered through a 100 μm cell strainer.

713   The cell suspensions were centrifuged at 50 × g for 1 min to segregate the cell fractions as

714   follows; the pellet and supernatant were collected as the hepatocyte fraction and

715   leukocyte/LSEC/HSC fraction, respectively. This procedure was repeated three times. Both

716   fractions were centrifuged at 400 × g for 7 min before FACS staining.

717

718   **Flow cytometry and cell sorting**

719   Cell-surface Fc receptors were blocked in anti-mouse CD16/32 antibody (1:250, #553141, BD

720   Bioscience) for 20 min at 4 °C before staining with FACS antibodies. Subsequently, the primary

721   antibodies were added. All antibodies, conjugates, lot numbers and dilution rates are listed in

722   **Supplementary Table 1**. For Marco staining, cells were stained with a primary unconjugated

723   antibody, followed by staining with a fluorophore-conjugated secondary antibody. The cells

724   were incubated for 30 min at 4°C for staining, followed by washing in PBS containing 2% FBS.

725   After centrifugation at 500 × g for 5 min, the cells were resuspended in autoMACS running

726   buffer. For intracellular cytokine staining, cells were stimulated for 5 h with 50 ng/mL phorbol

727   12-myristate 13-acetate (Sigma-Aldrich) and 500 ng/mL ionomycin (Sigma-Aldrich) in the

728   presence of 10 μg/mL Golgistop (BD Bioscience). Cell surface markers were stained first. After

729   washing with 2% FBS-containing PBS, fixation and permeabilisation were performed using an

730   Intracellular Fixation and Permeabilisation Buffer set (eBioscience™), followed by

731   intracellular cytokine staining. The cells were resuspended in autoMACS running buffer. Raw

732   data were obtained using FACS Celesta (BD Biosciences, USA) or SH800 cell sorter (Sony,

733   Japan) and analysed using FlowJo (BD Biosciences). Cell sorting was performed on the SH800

734   cell sorter. Gating strategies are shown in **Supplementary Fig. 7**.

735

736   **Single-cell RNA sequencing**

737   The 10× Genomics Chromium Controller was used to construct a single-cell RNA library and

738   sequence the single-cell suspension following the protocol outlined in the Chromium Single

739   Cell 3' Reagent Kit User Guide. We used the Chromium Next GEM Single Cell 3' Kit v3.1

740   (#PN-1000269; 10x Genomics), Chromium Next GEM Chip G Single Cell Kit (#PN-1000127;

741   10x Genomics), and Dual Index Kit TT Set A (#PN-1000215; 10× Genomics). According to

742   the manufacturer's recommendations, approximately 2,000 live cells per sample were loaded

743   onto the Chromium controller to generate 2,000 single-cell gel-bead emulsions for library

744   preparation and sequencing. Oil droplets of encapsulated single cells and barcoded beads

745   (GEMs) were subsequently reverse-transcribed in the Veriti Thermal Cycler (Thermo Fisher

746   Scientific), resulting in cDNA tagged with a cell barcode and unique molecular index. Next,

747   cDNA was amplified to generate single-cell libraries according to the manufacturer's protocol.

748   The Agilent Bioanalyzer High Sensitivity DNA assay (#5067-4626; Agilent) was used to

749   quantify the cDNA before it was enzymatically fragmented, end-repaired, and polyA-tagged.

750   Cleanup/size selection was performed on the amplified cDNA using SPRIselect magnetic beads

751   (#B23317, Beckman-Coulter). Next, Illumina sequencing adapters were ligated to the size-

752   selected fragments and purified using SPRIselect magnetic beads. Finally, sample indices were

753   selected and amplified, followed by double-sided size selection using SPRIselect magnetic

754   beads. The final library quality was assessed using the Agilent Bioanalyser High Sensitivity

755   DNA assay. The samples were then sequenced on the Illumina NovaSeq 6000 in paired-end

756   mode (read 1: 28 bp; read 2: 91 bp). The resulting raw reads were processed using 10×

757   Genomics CellRanger 4.0.0.

758

Processing of single-cell RNA sequencing data

760   R (version 4.1.2) and Seurat (version 4.1.1) were used for processing the single-cell

761   transcriptome data[70]. Unsupervised clustering and gene expression analysis were performed

762   according to the Seurat guidance. In brief, we omitted the genes and cells in the data based on

763   the following criteria: (1) the genes detected in fewer than five cells, (2) the cells with fewer

764   than 200 or more than 5,000 genes, and (3) the cells with more than 20% mitochondrial genes.

765   In mouse zone-specific single-cell RNA-seq, a total of 2,461 cells (including 1,282 cells and

766   1,179 cells from PV and CV zones, respectively) were selected for the subsequent analysis. In

767   a reanalysis of public human single-cell data, a total of 28,609 cells (including 16,786 and

768   11,823 cells from healthy and cirrhotic samples, respectively) were selected for the subsequent

769   analysis. Multiple data were integrated using the reciprocal principal components analysis

770   (RPCA)-based integration method, then linear dimensional reduction was performed using a

771   principal component analysis method. Cluster classification was performed using the nearest

772   neighbour graph-based clustering method, in which we tuned the dimensionality and resolution

773   parameters to determine the number of clusters. In the mouse analysis, 14 cell clusters were

774   initially obtained by setting the dimensionality to "1:15" and the resolution to "0.42." In the

775   human analysis, 14 cell clusters were initially obtained by setting the dimensionality to "1:15"

776   and the resolution to "0.2." Subsequently, we searched for marker genes for each cluster using

777   a 'FindAllMarkers' function and assign clusters to known cell types based on the markers

778   (**Supplementary Tables 2 and 3**) with reference to the previous reports[9,12,15,16,71–73]; however,

779   we omitted clusters that could not be assigned.

780

781   **Quantitative reverse transcription-polymerase chain reaction (qRT-PCR)**

782   Total RNA was extracted and purified using the RNeasy mini kit (#74106, Qiagen). cDNA was

783   prepared using Superscript III reverse transcriptase (#18080044, Invitrogen) following the

784   manufacturer's instructions. Real-time PCR was performed using TB Green Premix EX Taq

785　(#RR420W, TaKaRa) on a Thermal Cycler Dice Real Time System (TaKaRa, Japan). Relative

786　gene expression levels were calculated by the ΔΔCt method using *Gapdh* as an internal control.

787　The specific primer pairs (forward and reverse sequences, respectively) are listed in

788　**Supplementary Table 4**. *Gapdh* is a broadly acceptable choice as one of the stable

789　housekeeping genes for use in macrophages[74]. We also confirmed the validity of *Gapdh* by

790　comparing the results with that of other commonly used internal control genes, *18s*, *Rpl32*,

791　*B2m*, and *Ubc* (the data are shown in **Supplementary Fig. 8**). Furthermore, we validated the

792　accuracy of the qPCR results by conducting a multimodal analysis.

793

794　**Immunofluorescence staining and confocal imaging**

795　The livers were embedded in 4% paraformaldehyde (PFA) (#158127, Sigma) solution

796　overnight and then dehydrated using 15% and 30% sucrose solutions. The livers were cut into

797　small pieces and embedded in Tissue-Tek O.C.T.™ Compound. Frozen sections (20 μm

798　thickness) were cut using a CM3050S cryostat (Leica) and fixed on APS-coated slides

799　(Matsunami). The sections were permeabilised in 0.5% tween-20 (#P1379, Sigma) solution for

800　20 min at RT and blocked in 4% bovine serum albumin (BSA) (#A6003, Sigma) solution for

801　60 min. Subsequently, the sections were stained with antibodies diluted in PBS containing 0.1%

802　tween-20 and 1% BSA. The antibodies used for tissue staining are listed in **Supplementary**

803　**Table 1**. After staining, the slides were mounted in PBS and scanned on a confocal microscope

804   (A1R, Nikon) with a ×20 objective lens (CFI Plan Apo VC, numerical aperture: 0.75, Nikon).

805   Raw imaging data were processed using NIS elements (Nikon) and Imaris (Bitplane). Cell

806   counting and cellular morphological analysis were performed using Imaris with the Spot and

807   Surface functions, respectively.

808

809   **16S rRNA-sequencing of colorectal bacteria**

810   Colorectal contents were squeezed out from just below the cecum to the anus. The samples

811   were instantly frozen with liquid nitrogen. DNA was extracted from the samples using GENE

812   PREP STAR PI-1200 (Kurabo, Japan) according to the manufacturer's protocol. Each library

813   was prepared according to the Illumina 16S Metagenomic Sequencing Library Preparation

814   Guide with the primer set, 27Fmod: 5′AGRGTTTGATCMTGGCTCAG-3′ and 338R: 5′-

815   TGCTGCCTCCCGTAGGAGT-3′, targeting the V1–V2 regions of the 16S rRNA gene. Next,

816   251-bp paired-end sequencing of the amplicons was performed on a MiSeq system (Illumina)

817   using the MiSeq Reagent v2 500 cycle kit. The paired end sequences obtained were merged,

818   filtered, and denoised using DADA2. Taxonomic assignment was performed using a QIIME2

819   feature-classifier plugin with the Greengenes 13_8 database. The QIIME2 pipeline[75], version

820   2020.2, served as the bioinformatics environment for the processing of all relevant raw

821   sequencing data.

822

In vivo assay of MP2 Kupffer cell induction by Odoribacteraceae

To establish gnotobiotic mice, germ-free mice received 1×10^8 colony forming units (CFUs) of Odoribacteraceae (Odori) or *Bacteroides stercoris* (Stercoris) via oral gavage twice at days 0 and 2. Germ-free mice and gnotobiotic mice were then maintained in individual isolators, respectively, at the animal facilities of Oriental Bio Service, Inc. At day 21, the livers and colorectal contents of germ-free and gnotobiotic mice were harvested for the assays. For assessment of MP2 induction by SPF commensals or by combination of Odori/Stercoris and SPF commensals, mice were treated with ampicillin, vancomycin, neomycin, and metronidazole via drinking water for 6 weeks to deplete gut commensals and reduce MP2 population, and then Odori, Stercoris, or vehicle was inoculated into the mice. The mice were housed with SPF mice in the same cage. As for the inoculation of Odori and Stercoris, 1×10^8 CFUs of each bacterium was inoculated per mouse via oral gavage for the first 5 days consecutively, and thereafter, every other day until day 19. At day 21, the livers and colorectal contents were harvested for the assays.

Measurement of faecal isoallo-lithocholic acid concentration

Faecal contents were suspended in 10 times the volume of 2-propanol containing the internal standard (250 ng/mL LCA-d4). The suspension was homogenised using Precellys (Bertin Technologies) and then incubated for 30 min at 37 °C under sonication. The suspension was

52

842   centrifuged at 13,000 × g for 5 min at 4 °C. Supernatant was collected for LC-MS/MS analysis.

843   1 μL of the supernatant was used for the analysis. LC-MS/MS analysis was performed under

844   previously reported conditions[26] with slight modifications using a Nexera XR system

845   (Shimadzu, Japan) coupled with an LCMS-8050 triple quadrupole mass spectrometer

846   (Shimadzu) with a heated electrospray ionization source. A separation column, InertSustain

847   C18 (150 mm × 2.1 mm I.D., 3 μm; GL Sciences), was used at 40 °C. A mixture of 10 mM

848   ammonium acetate (A) and acetonitrile (B) was used as the mobile phase and the separation

849   was carried out by gradient elution at a flow rate of 0.2 mL/min. The gradient condition was as

850   follows: 14%B, 0–0.5 min; 14–22%B, 0.5–5 min; 22–28%B, 5–28 min; 28–54%B, 28–55 min;

851   54–98%B, 55–66 min; 98%B, 66–70 min; and 14%B, 70–75 min. To operate the LC-MS/MS

852   analysis, we used the following MS parameters: interface voltage, -3kV; interface temperature,

853   300 °C; desolvation line temperature, 250 °C; heat block temperature, 400 °C; nebulizing gas,

854   2 L/min; heating gas, 10 L/min; drying gas, 10 L/min. A deuterated internal standard （LCA-

855   d_4） was used to quantify isoallo-LCA. The data analysis was performed using LabSolutions,

856   ver. 5.120 (Shimadzu).

857

858   **Preparation of enhanced green fluorescent protein (eGFP)-labelled *E. coli* and in vivo**

859   **challenges**

860   We inserted eGFP DNA into multiple cloning sites of the bacterial vector pQE-60. *E. coli*

861   DH5α cells (#9057, TaKaRa) were transformed using this recombinant vector and then plated

862   on lysogeny broth medium (#20069-65, Nacalai) containing 100 µg/mL ampicillin (#19769-

863   64, Nacalai). Single eGFP-positive colonies were picked and further cultured in lysogeny broth

864   medium (#20068-75, Nacalai) containing 100 µg/mL ampicillin with agitation at 37°C for

865   propagation. The cell density of *E. coli* was measured using BioPhotometer Plus (Eppendorf,

866   Germany) and adjusted to an OD600 of 0.38–0.40. The *E. coli* culture medium (1 mL) was

867   collected and centrifuged at 10,000 × g for 5 min. The supernatant was discarded, and the pellet

868   was suspended in sufficient PBS to remove any released bacterial components. Subsequently,

869   the *E. coli* suspension was re-centrifuged at 10,000 × g for 5 min. The supernatant was

870   discarded, and the pellet was resuspended in 500 µL PBS. Then, 100 µL of the suspension was

871   slowly injected into the mice via the PV using an ultra-fine 29 G insulin syringe (#SS-

872   10M2913A, TERUMO). Thereafter, the liver was immediately harvested and fixed in 4% PFA

873   before immunofluorescence staining.

874

875   **In vitro assay of bacterial capture by liver-resident macrophages**

876   The eGFP-labelled *E. coli* density was measured using BioPhotometer Plus and adjusted to

877   an OD600 of 0.19 – 0.21. The *E. coli* culture medium (1 mL) was collected, and 400 µL of an

878   *E. coli*-containing PBS suspension was prepared as described above. Intrahepatic immune cells

879   were collected from the liver (see above), and Kupffer cells were plated onto a 6-well glass-

880   bottom dish (#5816-006, Iwaki) in 3 mL Dulbecco's Modified Eagle Medium (#08459-64,

881   Nacalai) containing 2% FBS and 10 ng/mL macrophage colony-stimulating factor (#315-02,

882   Peprotech) at 37°C for 2 h to allow the Kupffer cells to adhere to the bottom. The cells were

883   then washed to remove any non-adhering cells. The *E. coli* (150 µL) suspension was added to

884   the Kupffer cells and incubated for 1 h at 37°C to allow the Kupffer cells to capture the *E. coli*.

885   Subsequently, the cells were washed and incubated in cell dissociation Hank's solution (#S-

886   004-B, Millipore) for 10 min at 37°C for collection. The cells were then stained with CD45-

887   PE/Cy7, CD64-PerCP/Cy5.5, F4/80-APC, and MARCO-DyLight405 (see **Supplementary**

888   **Table 1**) and analysed using BD FACS Celesta and FlowJo software.

889

890   **Experimental colitis model**

891   The mice received 1% dextran sodium sulphate (DSS, #160110, MP Biomedicals) via

892   drinking water for 7 days, followed by untreated normal water for 4 days to induce acute

893   colitis[76]. The mice were used for the assays 11 days after starting DSS treatment. Mouse body

894   weights were measured on days 0, 7, and 11. To generate the chronic colitis model, the mice

895   received three cycles of 1% DSS via drinking water for 7 days, followed by untreated normal

896   water for 7 days[77]. After the third DSS treatment, normal water was given for 4 days. The livers

897   were harvested for the assays 39 days after the start of the first DSS treatment. Mouse body

898   weights were measured on days 0, 7, 14, 21, 28, 35, and 39.

Diet-induced NAFLD/NASH model

900

901 Mice were fed ad libitum for up to 8 weeks with a 0.1 % methionine and choline-deficient

902 high-fat (60 kcal%) diet[78,79] (Research Diets, A06071302) to induce the non-alcoholic fatty

903 liver disease and steatohepatitis (NAFLD/NASH). Peripheral blood and livers were harvested

904 every 2 weeks for the assays. Serum samples were prepared for the biochemical analyses. Liver

905 samples were fixed in 4 % paraformaldehyde for 2 days. Some parts were embedded in paraffin,

906 and the others were dehydrated with 15% and 30% sucrose solutions and embedded in O.C.T.

907 Compound. Paraffin-embedded livers were used for Masson trichrome staining and O.C.T.

908 Compound-embedded frozen livers were used for immunofluorescence staining.

909

Human samples and immunofluorescence staining

910

911 The Institutional Review Board for Clinical Research at Osaka University Hospital approved

912 this study. Informed consent for surgical intervention was obtained from each patient. Control

913 or PSC liver tissues, located far from any colorectal cancer metastatic lesion, were obtained

914 from patients who underwent surgical resection at Osaka University Hospital. These tissue

915 specimens were immediately fixed in 10% formalin and then processed routinely for paraffin

916 embedding. Paraffin-embedded sections were cut at a thickness of 4 μm, deparaffinised in

917 cresol and ethanol, and rinsed in PBS. Antigens were retrieved by heating with EnVision FLEX

918   Target Retrieval Solution, High pH (Dako, Agilent) at 110 °C for 15 min. After washing in

919   deionised distilled water and EnVision FLEX Wash Buffer (Dako, Agilent), the sections were

920   incubated in Antibody Diluent/Block (Akoya Biosciences) for 30 min at RT. Primary antibodies

921   were diluted in the Antibody Diluent/Block. After incubation with antibodies at 4 °C overnight,

922   the sections were washed in Wash Buffer, incubated with Opal Polymer HRP Ms + Rb (Akoya

923   Biosciences) for 30 min at RT, and washed in Wash Buffer. Next, the sections were incubated

924   with Opal fluorophores (Akoya Biosciences) for 10 min, then washed in Wash Buffer and

925   rinsed in PBS. For the subsequent antibody applications, the slides were heated again to remove

926   the antibody complexes after incubation, followed by the steps described above. Finally, after

927   heating, the slides were washed with Wash Buffer and then cover-slipped in Fluoro-KEEPER

928   Antifade Reagent, Non-Hardening Type with DAPI (Nacalai Tesque). The primary antibodies

929   used included anti-MARCO (Sigma-Aldrich) (1:500 dilution), anti-CD68 (Dako, Agilent)

930   (1:100 dilution), and anti-CK19 (Cell Marque) (1:100 dilution). The fluorophores used

931   included Opal 690, Opal 570, and Opal 520 at 1:100 dilution in 1 × Plus Amplification Diluent

932   (Akoya Biosciences). Imaging was performed using a confocal microscope (A1R, Nikon) with

933   a ×20 objective lens (CFI Plan Apo VC, numerical aperture: 0.75, Nikon). The antibodies used

934   for human tissue staining are listed in **Supplementary Table 1**.

935

936   **Statistics and Reproducibility**

937   All line graphs are presented as means ± standard error of the mean (SEM). All box plots

938   present the means, medians, smallest observations, lower and upper quartiles, and largest

939   observations. Basically, nonparametric paired and unpaired two-sided Mann–Whitney U tests

940   were applied for comparisons between the two groups. Statistical analyses were performed

941   using R (version 4.1.2). Experiments were repeatedly performed to ensure the reproducibility

942   of our observations. All results were determined from at least two independent experiments

943   (twice: Figs. 1e-h, 2a, 4a-d, f, Extended Data Figs. 5a-h, 6a-h, 7a-c, 10a-c, 11b-d, g-j,

944   Supplementary Figs. 1a-c, 2a-c, 3d, 8a-d, and three or more times: Figs. 1a-d, i, 2b-d, 3a-f, 4e,

945   g, h, 5b-i, Extended Data Figs. 1a, b, 2c-e, 4a-c, 7e, f, 8b-e, 9b-p, 11f, Supplementary Figs. 2d,

946   e, 3c, 4a-d, 5a-c).

947

948   **Data availability**

949   Visium and single-cell RNA sequencing data have been deposited in the NCBI Gene

950   Expression Omnibus (GEO) database under the accession numbers GSE213388 and

951   GSE213165 [https://www.ncbi.nlm.nih.gov/geo/query/acc.cgi], respectively. For the

952   reanalysis of mouse liver single-cell RNA sequencing and Visium, we obtained the datasets

953   from the GEO (the accession number: GSE192742 and URL:

954   https://www.ncbi.nlm.nih.gov/geo/query/acc.cgi)[9]. For the reanalysis of human single-cell

955   RNA sequencing, we obtained the data of human liver CD45$^+$ cells from eight patients (four

956   normal and four cirrhotic livers) from the GEO (the accession numbers: GSM4041150,

957   GSM4041153, GSM4041155, GSM4041160, GSM4041161, GSM4041166, GSM4041168,

958   GSM4041169 and URL: https://www.ncbi.nlm.nih.gov/geo/query/acc.cgi?acc=GSE136103)[15].

959   For the reanalysis of mouse liver and intestine single-cell RNA sequencing, we obtained the

960   datasets from Mouse Cell Atlas[80] [https://bis.zju.edu.cn/MCA/]. All other data in this study are

961   available from the corresponding author upon reasonable request.

962

963   **Code availability**

964   All source codes for the Visium and single-cell analyses are available from the GitHub

965   repository [https://github.com/OU-ICB/YMiyamoto2023].

Methods references

966

967 51. Adachi, O. *et al.* Targeted disruption of the MyD88 gene results in loss of IL-1- and IL-

968 18-mediated function. *Immunity* **9**, 143–150 (1998).

969 52. Victora, G. D. *et al.* Germinal center dynamics revealed by multiphoton microscopy

970 with a photoactivatable fluorescent reporter. *Cell* **143**, 592–605 (2010).

971 53. Madisen, L. *et al.* A robust and high-throughput Cre reporting and characterization

972 system for the whole mouse brain. *Nat. Neurosci.* **13**, 133–140 (2010).

973 54. Arredouani, M. *et al.* The scavenger receptor MARCO is required for lung defense

974 against pneumococcal pneumonia and inhaled particles. *J. Exp. Med.* **200**, 267–272

975 (2004).

976 55. Atarashi, K. *et al.* Induction of colonic regulatory T cells by indigenous Clostridium

977 species. *Science* **331**, 337–341 (2011).

978 56. Faust, N., Varas, F., Kelly, L. M., Heck, S. & Graf, T. Insertion of enhanced green

979 fluorescent protein into the lysozyme gene creates mice with green fluorescent

980 granulocytes and macrophages. *Blood* **96**, 719–726 (2000).

981 57. Jung, S. *et al.* Analysis of fractalkine receptor CX_3CR1 function by targeted deletion

982 and green fluorescent protein reporter gene insertion. *Mol. Cell. Biol.* **20**, 4106–4114

983 (2000).

984 58. Kamran, P. *et al.* Parabiosis in mice: a detailed protocol. *J. Vis. Exp.* 1–5 (2013).

985   59.   Tavares, A. J. *et al.* Effect of removing Kupffer cells on nanoparticle tumor delivery.

986   *Proc. Natl. Acad. Sci. U. S. A.* **114**, E10871–E10880 (2017).

987   60.   Xu, M. *et al.* c-MAF-dependent regulatory T cells mediate immunological tolerance to

988   a gut pathobiont. *Nature* **554**, 373–377 (2018).

989   61.   Ogawa, Y. *et al.* Gut microbiota depletion by chronic antibiotic treatment alters the

990   sleep/wake architecture and sleep EEG power spectra in mice. *Sci. Rep.* **10**, 19554

991   (2020).

992   62.   Hie, B., Bryson, B. & Berger, B. Efficient integration of heterogeneous single-cell

993   transcriptomes using Scanorama. *Nat. Biotechnol.* **37**, 685–691 (2019).

994   63.   Wolf, F. A., Angerer, P. & Theis, F. J. SCANPY: large-scale single-cell gene expression

995   data analysis. *Genome Biol.* **19**, 15 (2018).

996   64.   Huang, D. W., Sherman, B. T. & Lempicki, R. A. Systematic and integrative analysis

997   of large gene lists using DAVID bioinformatics resources. *Nat. Protoc.* **4**, 44–57 (2009).

998   65.   Schneider, C. A., Rasband, W. S. & Eliceiri, K. W. NIH Image to ImageJ: 25 years of

999   image analysis. *Nat. Methods* **9**, 671–675 (2012).

1000   66.   Lämmermann, T. *et al.* Neutrophil swarms require LTB4 and integrins at sites of cell

1001   death in vivo. *Nature* **498**, 371–375 (2013).

1002   67.   Uderhardt, S., Martins, A. J., Tsang, J. S., Lämmermann, T. & Germain, R. N. Resident

1003   macrophages cloak tissue microlesions to prevent neutrophil-driven inflammatory

1004   damage. *Cell* **177**, 541-555 (2019).

1005   68.   Medaglia, C. *et al.* Spatial reconstruction of immune niches by combining

1006   photoactivatable reporters and scRNA-seq. *Science* **358**, 1622–1626 (2017).

1007   69.   Bonnardel, J. *et al.* Stellate cells, hepatocytes, and endothelial cells imprint the Kupffer

1008   cell identity on monocytes colonizing the liver macrophage niche. *Immunity* **51**, 638-

1009   654 (2019).

1010   70.   Hao, Y. *et al.* Integrated analysis of multimodal single-cell data. *Cell* **184**, 3573-3587

1011   (2021).

1012   71.   Xiong, X. *et al.* Landscape of intercellular crosstalk in healthy and NASH liver revealed

1013   by single-cell secretome gene analysis. *Mol. Cell* **75**, 644-660 (2019).

1014   72.   Aizarani, N. *et al.* A human liver cell atlas reveals heterogeneity and epithelial

1015   progenitors. *Nature* **572**, 199–204 (2019).

1016   73.   Liew, P. X., Lee, W.-Y. & Kubes, P. iNKT cells orchestrate a switch from inflammation

1017   to resolution of sterile liver injury. *Immunity* **47**, 752-765 (2017).

1018   74.   Ju, W. *et al.* Reference gene selection and validation for mRNA expression analysis by

1019   RT-qPCR in murine M1- and M2-polarized macrophage. *Mol. Biol. Rep.* **47**, 2735–2748

1020   (2020).

1021   75.   Bolyen, E. *et al.* Reproducible, interactive, scalable and extensible microbiome data

1022   science using QIIME 2. *Nat. Biotechnol.* **37**, 852–857 (2019).

1023   76.   Mathies, F. *et al.* Colitis promotes a pathological condition of the liver in the absence of

1024   Foxp3^{+} regulatory T cells. *J. Immunol.* **201**, 3558–3568 (2018).

1025   77.   Kwon, J., Lee, C., Heo, S., Kim, B. & Hyun, C.-K. DSS-induced colitis is associated

1026   with adipose tissue dysfunction and disrupted hepatic lipid metabolism leading to

1027   hepatosteatosis and dyslipidemia in mice. *Sci. Rep.* **11**, 5283 (2021).

1028   78.   Matsumoto, M. *et al.* An improved mouse model that rapidly develops fibrosis in non-

1029   alcoholic steatohepatitis. *Int. J. Exp. Pathol.* **94**, 93–103 (2013).

1030   79.   Ikawa-Yoshida, A. *et al.* Hepatocellular carcinoma in a mouse model fed a choline-

1031   deficient, L-amino acid-defined, high-fat diet. *Int. J. Exp. Pathol.* **98**, 221–233 (2017).

1032   80.   Fei, L. *et al.* Systematic identification of cell-fate regulatory programs using a single-

1033   cell atlas of mouse development. *Nat. Genet.* **54**, 1051–1061 (2022).

1034

Author contributions

Y.M. conceived the original idea of this study. Y.M. and M.I. devised the concrete concept.

Y.M., J.Kikuta, and M.I. designed the experiments. Y.M. conducted all of the experiments and

64

1054 data analyses with assistance from J.Kikuta, T.M., T.H., K.F., Y.U. and E.Y. D.M. and D.O.

1055 processed the sequence data. Y.C.L., S.S. and D.O. established a new data processing method

1056 for spatial transcriptomics. S.K. and H.E. collected and provided the human liver samples and

1057 T.M. and E.M. performed the immunofluorescence staining. K. Tryggvason generated *Marco*⁻

1058 *⁻* mice. T.S. maintained them and assisted with experiments using *Marco* knockout mice. K.A.

1059 and K.H. isolated and provided *Odoribacteraceae* Strain#21. T.Y. and J.Kunisawa measured

1060 concentrations of isoallo-lithocholic acid in faeces. H.K. and K. Takeda supervised the

1061 experiments and analyses pertaining to gut commensal microbes. Y.M. wrote the initial draft,

1062 and Y.M., J.Kikuta and M.I. revised the final draft.

1063

1064 **Competing interests**

1065 The authors declare no competing financial interests.

1066

1067 **Additional information**

1068 Supplementary Information is available for this paper.

1069 Correspondence and requests for materials should be addressed to Masaru Ishii

1070 (**mishii@icb.med.osakau.ac.jp**)

1071   **Extended Data Figure Legends**

1072

1073   **Extended Data Fig. 1. Spatial heterogeneity in neutrophil adhesion in the steady-state**

1074   **liver. a**, Representative intravital image [left, green: neutrophils, red: Qtracker655 (blood

1075   vessels), and blue: SHG (tissue collagens)] and neutrophil tracks (right, individual colours

1076   mean individual cell tracks). Tracks of neutrophils that adhered to the tissue for over 10 min

1077   are shown. Scale bar: 100 μm. **b,** Numbers of the neutrophil tracks within each zones (n = 7).

1078   The quantitative data are presented as means (asterisk) with medians, smallest observations,

1079   lower and upper quartiles, and largest observations. Statistical significance was determined

1080   using unpaired two-sided Mann–Whitney U test.

1081

1082 **Extended Data Fig. 2. Spatial heterogeneity in monocyte/macrophage responses to the**

1083 **laser-induced tissue damage in the liver. a**, Timeline of neutrophil and monocyte responses

1084 post the laser-induced tissue damage. **b**, Experimental design to quantify

1085 monocyte/macrophage accumulations at the laser-induced damaged sites. **c,d**, Representative

1086 intravital images of in situ inflammatory responses by monocytes/macrophages upon the laser-

1087 induced damages under control (c, n = 13) and clodronate liposome-treated (resident

1088 macrophage-depleted) conditions (d, n = 10) [green: monocytes/macrophages, white: damaged

1089 sites (autofluorescence), and blue: SHG (tissue collagens)]. Scale bar: 100 μm. Quantified

1090 accumulation scores of monocyte/macrophage at the lesions are shown (right). **e**, PV/CV ratio

1091 of monocyte/macrophage accumulation at 24 h post-laser ablation under control (n = 13) and

1092 resident macrophage-depleted (n = 10) conditions, indicating spatial polarisation of

1093 accumulation: > 1 and < 1 indicate bias towards PV and CV zones, respectively. All quantitative

1094 data are presented as means (asterisk) with medians, smallest observations, lower and upper

1095 quartiles, and largest observations. Statistical significance was determined using paired (**c, d**)

1096 and unpaired (**e**) two-sided Mann–Whitney U tests.

Extended Data Fig. 3. Reanalysis to identify the Marco$^+$ Kupffer cell subset (MP2) using public mouse and human databases. a, Reproduction of Uniform Manifold Approximation and Projection (UMAP) depicting distinct myeloid cell clusters identified in the mouse liver cell atlas. The Kupffer cell cluster was further analysed for isolating subclusters. **b**, Density of *Marco*- (left) and *Il10*- (right) expressing cells in each Kupffer cell subcluster. Subclusters 8, 10 and 17 should be the MP2. **c**, Reproduction of UMAP depicting the liver zonation in the mouse liver cell atlas. **d**, Density of *Marco$^+$ Clec4f$^+$* spots on the liver zonation plot (left). Violin plot showing quantification of the densities in each zone (right). Statistical significance was determined using one-sided Student's t-test and resultant *p*-values were corrected using the Benjamini-Hochberg method. **e**, Summary of human sample information (left). tSNE plot depicting distinct immune cell clusters (right). All single-cell data from healthy and cirrhotic samples were integrated and represented on the same tSNE plot. Each cluster was assigned to the known cell types based on marker genes (**Supplementary Table 3**). The numbers in brackets indicate the cluster number. Resident macrophages include three clusters. **f**, Gene expression of *CD68* (left), a human macrophage marker, *MARCO* (centre), and *IL10* (right) was visualised with an R package 'Nebulosa' (Kernel Gene-Weighted Density Estimation). **g**, Percentage of MARCO$^+$ IL10$^+$ cells to total macrophages under healthy and cirrhotic conditions. Data are presented as means (asterisk) with medians, smallest observations, lower

1116   and upper quartiles, and largest observations. Statistical significance was determined using

1117   unpaired two-sided Mann–Whitney U test.

1118

Extended Data Fig. 4. Relationship between Marco and IL-10 expressions in Kupffer cells.

a, Transcriptional activity of *Il10* in Marco⁻ (MP1) and Marco⁺ (MP2) Kupffer cells visualised using *Il10*-Venus mice (n = 7). To confirm the background noise, we used wild-type mice as the negative control (n = 5). Venus expression was detected using AlexaFluor647-conjugated anti-Venus antibody to avoid the influence of autofluorescence. Mean fluorescence intensity (MFI) of AlexaFluor647 (from *Il10*-venus) was measured for statistical comparison. **b**, Correlation between Marco and Il10-venus expressions. 'R' indicates the correlation coefficient. The error bands mean 95% confidence interval. **c**, Relative mRNA expression of *Il10*, *Il1rn* and *Tgfb1* to *Gapdh* in total Kupffer cell fraction from *Marco*^{+/+} control (n = 7-9) and *Marco*^{−/−} (n = 5-9) mice. All data are presented as means (asterisk) with medians, smallest observations, lower and upper quartiles, and largest observations. Statistical significance was determined using unpaired two-sided Mann–Whitney U test.

1131

Extended Data Fig. 5. Interleukin-10 signalling in PV zones suppressively regulates ICAM1-integrin interactions between endothelial cells and neutrophils. a, Representative flow cytometry gating to identify the liver sinusoidal endothelial cell (LSEC) subsets. The histogram shows the ICAM-1 expression levels on each subset. **b**, Mean fluorescence intensity (MFI) from ICAM-1 on CD117$^+$ and CD117$^-$ LSECs (n = 4). **c**, Representative immunofluorescence images of ICAM-1 in the liver tissue (n = 4, blue: E-cadherin$^+$ PV zones, green: ICAM-1). PV, portal vein; CV, central vein. Scale bar : 100 μm. **d**, MFI from ICAM-1 on CD117$^+$ and CD117$^-$ LSECs under anti-IL10R and isotype control antibody-treated conditions (n = 9 and 7, respectively). **e**, Fold changes of *Cxcl1* and *Cxcl2* mRNA expressions to *Gapdh* in CD117$^+$ LSECs, CD117$^-$ LSECs, and Kupffer cells from anti-IL10R and isotype control antibody-treated mice (n = 7 and 6, respectively). Data were standardized to ensure a control group mean value of '1'. **f–h**, Analyses of infiltrating neutrophils in the liver under anti-IL10R and isotype control antibody-treated conditions (n =4, respectively). Representative staining of integrin αM (Mac-1 or CD11b) on CD45$^+$ Mac-1$^+$ Ly-6G$^+$ neutrophils (f), percentage of Mac-1^{high} neutrophils (g), and absolute number of neutrophils (h). All data are presented as means (asterisk) with medians, smallest observations, lower and upper quartiles, and largest observations. Statistical significance was determined using unpaired two-sided Mann–Whitney U test.

1150

1151 **Extended Data Fig. 6. In vitro and in vivo assays of *E. coli*-capturing activity of MP1 and**

1152 **MP2 Kupffer cells. a**, Experimental design for in vitro bacteria-capture assay. **b**,

1153 Representative flow cytometry gating for identifying Marco$^-$ (MP1) and Marco$^+$ (MP2)

1154 Kupffer cells, and comparison of *E. coli*-derived fluorescence signals. **c**, Mean fluorescence

1155 intensity (MFI) of *E. coli*-derived GFP signals in MP1 and MP2 (n = 7). **d**, Experimental design

1156 for in vivo bacteria-capture assay. **e**, Representative immunofluorescence images (n = 3, 9

1157 visual fields, white: *E. coli*, red: F4/80$^+$ macrophages, blue: E-cadherin$^+$ PV zones) showing *E.*

1158 *coli* localisation in the liver (left and centre). Scale bar: 100 μm. Percentage of *E. coli* numbers

1159 within each zone to total *E. coli* (right). The exact *p*-value is 4.114×10^{-5}. **f**, Representative

1160 immunofluorescence images (n = 3, 15 visual fields, white: *E. coli*, blue: Marco$^-$ MP1, and

1161 red: Marco$^+$ MP2) showing the *E. coli*-capturing capability of each subset (left). The raw

1162 images were processed using the Imaris software (centre, yellow: *E. coli*, blue: Marco$^-$ MP1,

1163 and red: Marco$^+$ MP2). Scale bar: 100 μm. Percentage of *E. coli*-capturing Marco$^-$ MP1 and

1164 Marco$^+$ MP2 to total *E. coli*-capturing cells (right). **g**, Percentage of cells engulfing more than

1165 two *E. coli* in each Kupffer cell subset. **h**, Representative images showing *E. coli* localisation

1166 in the *Marco*$^{+/+}$ (n = 5, 25 visual fields) and *Marco*$^{-/-}$ (n = 4, 30 visual fields) livers (left,

1167 yellow: *E. coli*, blue: E-cadherin$^+$ PV zones). *E. coli* are shown as spherical spots using the

1168 imaris. Scale bar: 100 μm. Percentage of *E. coli* numbers within each zone to total *E. coli*

1169   (right). The exact p-values are 1.376×10^{-6} (PV) and 1.376×10^{-6} (CV). Data are presented as

1170   means (asterisk) with medians, smallest observations, lower and upper quartiles, and largest

1171   observations. Statistical significance was determined using paired (c) and unpaired (e-h) two-

1172   sided Mann–Whitney U test.

1173

1174 **Extended Data Fig. 7. Identification of gut commensal bacteria that induce MP2 Kupffer**

1175 **cells and involvement of gut commensals in MP2 induction by isoallo-lithocholic acids. a,**

1176 Relative abundance (%) of microbes at the family level (n = 6 and 5 for the SPF-A and SPF-B

1177 groups, respectively). The data were obtained by 16S rRNA-sequencing. **b,** Relative abundance

1178 (%) of each bacterium significantly enriched in "SPF-A" colorectal contents (n = 6 and 5 for

1179 the SPF-A and SPF-B groups, respectively). **c,** Correlation between the relative abundance of

1180 bacterium and the percentage of Marco$^+$ Kupffer cells (MP2). 'R' indicates the correlation

1181 coefficient. **d,** Graphical protocol for isoallo-lithocholic acid (isoalloLCA) and/or antibiotic

1182 treatments. **e,** Percentage of Marco$^+$ cells to total Kupffer cells under DMSO (n = 10),

1183 isoalloLCA (n = 10), and antibiotic/isoalloLCA (n = 13) treatments. **f,** Fold changes of *Il10*

1184 mRNA expression in total Kupffer cells under each condition [DMSO (n = 10), isoalloLCA (n

1185 = 10), and antibiotics/isoalloLCA (n = 9)]. Data were standardized to ensure a control group

1186 mean value of '1'. All data are presented as means (asterisk) with medians, smallest

1187 observations, lower and upper quartiles, and largest observations. Statistical significance was

1188 determined using unpaired two-sided Mann–Whitney U test.

1189

1190 **Extended Data Fig. 8. Periportal immunosuppressive Kupffer cells protect against gut**

1191 **commensal-driven liver inflammation related to experimental colitis. a,** Experimental

74

1192 design; *Marco*$^{+/+}$ and *Marco*$^{-/-}$ mice received 1% dextran sodium sulphate (DSS) via drinking

1193 water for 7 days to induce acute colitis, followed by drinking normal water for 4 days for

1194 recovery. On day 11, the livers were harvested for assays. **b**, Relative mRNA expression of

1195 anti-inflammatory cytokines *Il10* and *Il1rn* in Kupffer cells from *Marco*$^{+/+}$ and *Marco*$^{-/-}$ mice

1196 (n = 6 each). **c**, Representative intravital images of infiltrating inflammatory neutrophils in

1197 *Marco*$^{+/+}$ (left) and *Marco*$^{-/-}$ (right) mice (n = 6 each, green: neutrophils, red: vascular

1198 structures visualised by Qtracker655). Scale bar: 100 μm. **d**, Quantification of neutrophil

1199 numbers in 100 μm^3 tissues (n = 6, 12 visual fields per condition). Data contain two tissue

1200 sections from different lobes per mouse. **e**, Body weight change showing the percentage of

1201 body weight on day 11 to the original body weight (on day 0) (n = 6 each). All quantitative data

1202 are presented as means (asterisk) with medians, smallest observations, lower and upper

1203 quartiles, and largest observations. Statistical significance was determined using unpaired two-

1204 sided Mann–Whitney U test.

Extended Data Fig. 9. Periportal immunosuppressive Kupffer cells suppress progression of the non-alcoholic fatty liver disease. a, Analysis schedule. **b**, Representative Marco and TIM-4 staining in $CD45^+ CX_3CR1^- F4/80^+ CD64^+$-gated macrophages. **c,d,f,h**, Kinetics of the frequency of $Marco^+ TIM-4^+$ MP2 Kupffer cells (c), serum AST (d), serum ALT (f), and neutrophil abundance (h) [Healthy (n = 6-7), NAFLD/NASH 2W (n = 9-12), 4W (n = 11-12) and 6W (n = 8)]. **e,g,i**, Correlation between MP2 frequency and AST (e), ALT (g), and neutrophil abundance (i) in NAFLD/NASH 2W. 'R' indicates the correlation coefficient. The error bands mean 95% confidence interval. **j**, Serum AST and ALT levels in NAFLD/NASH-induced $Marco^{+/+}$ (n = 12, 12, 8 for 2W, 4W, 6W, respectively) and $Marco^{-/-}$ mice (n = 8, 10, 8 for 2W, 4W, 6W, respectively). **k**, Representative Masson trichrome staining of healthy $Marco^{+/+}$, NAFLD/NASH-induced $Marco^{+/+}$ and $Marco^{-/-}$ livers. Scale bar: 200 μm. **l**, Percentage of area occupied by fat droplets around portal veins in NAFLD/NASH 6W: $Marco^{+/+}$ (n = 5, 8 visual fields) and $Marco^{-/-}$ (n = 5, 10 visual fields). **m**, AST/ALT ratio in NAFLD/NASH 6W: $Marco^{+/+}$ and $Marco^{-/-}$ mice (n = 8 each). **n**, Representative immunofluorescence images showing MARCO (green), CD68 (red), and CK19 (cyan) in human livers: NAFLD/NASH (n = 7, 21 visual fields) and normal controls (n = 9, 27 visual fields). Scale bar: 100 μm. **o**, Absolute numbers of CD68-positive cells (macrophages) per visual field. **p**, Percentage of Marco-positive cells to total macrophages. All curve graphs

1224   represent means ± standard error of the mean (SEM). All box plots represent means (asterisk)

1225   with medians, smallest observations, lower quartiles, upper quartiles, and largest observations.

1226   Statistical significance was determined using unpaired two-sided Mann–Whitney U test. The

1227   exact p-values are 3.969×10^{-5} (h), 7.693×10^{-5} (p, Normal vs NAFLD), 5.114×10^{-10} (p,

1228   Normal vs NASH).

1229

1230 **Extended Data Fig. 10. Marco$^+$ Kupffer cells (MP2) belong to the CD206$^-$ ESAM$^-$ KC1**

1231 **subset. a**, Representative staining of CD206 and ESAM on Marco$^+$ and Marco$^-$ Kupffer cells

1232 (CD45$^+$ CX$_3$CR1$^-$ F4/80$^+$ CD64$^+$ population). **b**, Percentage of Marco$^+$ cells in KC1 and KC2

1233 (n = 4). **c**, Percentage of total Marco$^+$ Kupffer cells, Marco$^+$ KC1, and Marco$^+$ KC2 in all

1234 Kupffer cells (n = 4). **d**, Diagram illustrating the relationship between KC1/KC2 and MP1/MP2

1235 classifications of Kupffer cells. All box plots represent means (asterisk) with medians, smallest

1236 observations, lower quartiles, upper quartiles, and largest observations. Statistical significance

1237 was determined using unpaired two-sided Mann–Whitney U test.

1238

Extended Data Fig. 11. Marco$^+$ immunosuppressive Kupffer cells are supplied by embryo-derived macrophages. a, Experimental design; generating a parabiosis model to examine the differentiation from bone marrow-derived monocytes into Marco$^+$ Kupffer cells (MP2). **b**, Representative flow cytometry gating of tdTomato$^+$ cells on CD45$^+$ CX$_3$CR1$^-$ F4/80$^+$ CD64$^+$ cells in the liver from wild-type parabionts (left). Percentages of Marco$^-$ (MP1) and Marco$^+$ (MP2) cells to Tomato$^+$ Kupffer cells (right, n = 7). **c**, Representative immunofluorescence images of a wild-type parabiont liver [blue: E-cadherin (PV zones), white: tdTomato (bone marrow-derived macrophages), red: F4/80 (Kupffer cells), and green: Marco (MP2)]. Scale bar: 100 μm (large image) and 20 μm (zoomed images). **d**, Representative immunofluorescence images of a wild-type parabiont liver [white: tdTomato (bone marrow-derived macrophages), red: CD68 (Kupffer cells), and green: TIM-4 (resident Kupffer cells)]. Scale bar: 100 μm. **e**, Graphical protocol for analysing resident and bone marrow-derived (repopulated) Kupffer cells. **f**, Representative gating of Kupffer cells in clodronate liposome (CLL)-treated (on day 2) and untreated mice (left). Absolute number of TIM-4$^+$ resident Kupffer cells [right, control (n = 7) and CLL-treated (n = 6)]. **g**, Representative staining of Marco and TIM-4 on Kupffer cells in CLL-treated (on week 6) and untreated control mice. **h**, Absolute numbers of TIM-4$^+$ resident Kupffer cells (left) and TIM-4$^-$ bone marrow-derived Kupffer cells (right) in CLL-treated (on week 6, n = 12) and untreated control (n = 7) mice. The exact p-value is 3.969×10^{-5}. **i**,

79

1257   Percentage of Marco$^+$ cells in TIM-4$^+$ and TIM-4$^-$ Kupffer cells in CLL-treated mice (on week

1258   6, n = 12). **j**, Relative mRNA expression of *Il10* to *Gapdh* in TIM-4$^+$ and TIM-4$^-$ Kupffer cells

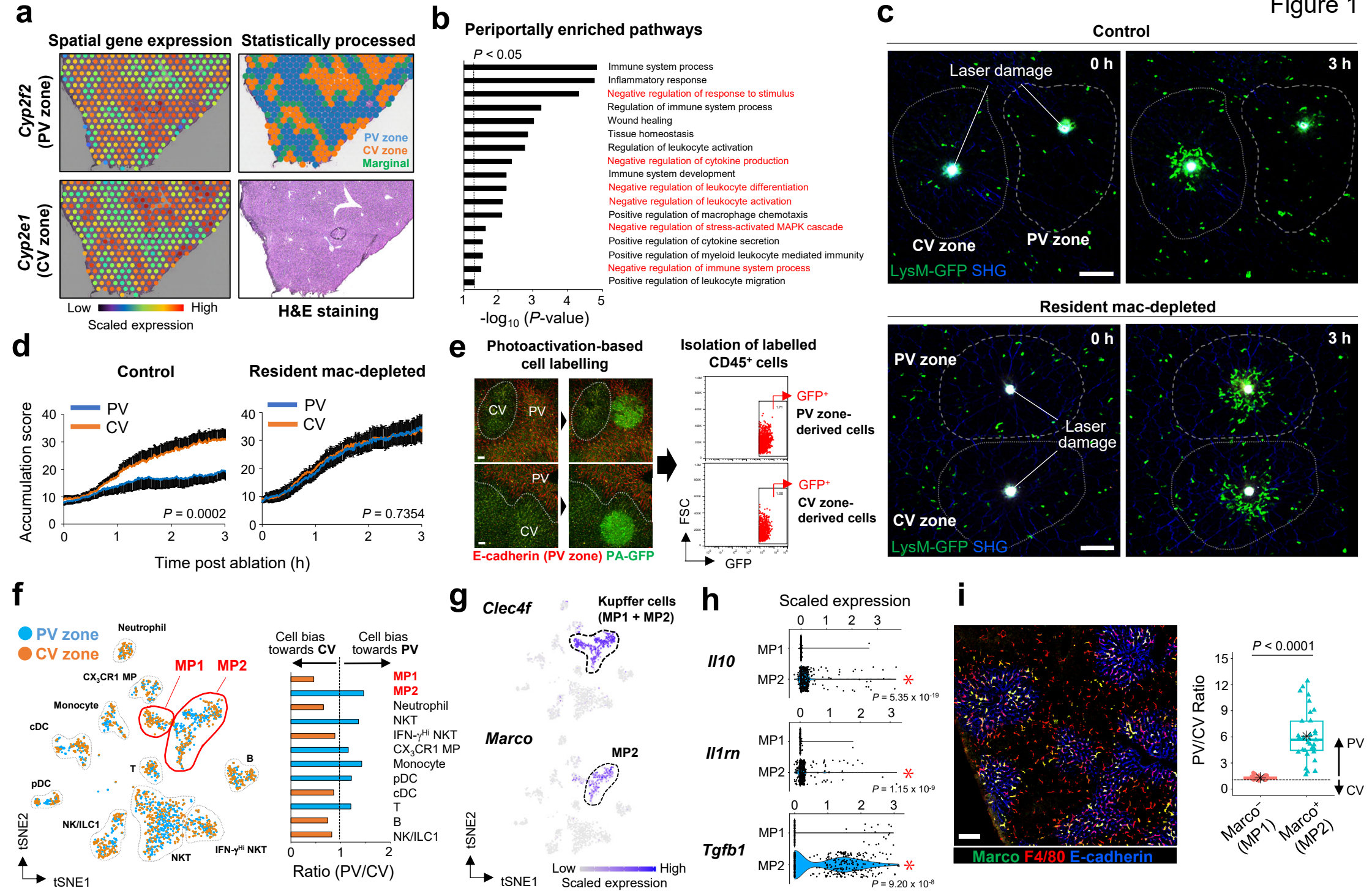1259   from CLL-treated mice (on week 6, n = 8). All data are presented as means (asterisk) with

1260   medians, smallest observations, lower and upper quartiles, and largest observations. Statistical

1261   significance was determined using unpaired (b, f, h) and paired (i, j) two-sided Mann–Whitney

1262   U test.

Figure 1

a Spatial gene expression | Statistically processed

Cyp2f2 (PV zone) — *Cyp2e1* (CV zone)

PV zone | CV zone | Marginal

H&E staining

Low — High
Scaled expression

b Periportally enriched pathways

$P < 0.05$

Immune system process
Inflammatory response
Negative regulation of response to stimulus
Regulation of immune system process
Wound healing
Tissue homeostasis
Regulation of leukocyte activation
Negative regulation of cytokine production
Immune system development
Negative regulation of leukocyte differentiation
Negative regulation of leukocyte activation
Positive regulation of macrophage chemotaxis
Negative regulation of stress-activated MAPK cascade
Positive regulation of cytokine secretion
Positive regulation of myeloid leukocyte mediated immunity
Negative regulation of immune system process
Positive regulation of leukocyte migration

$-\log_{10}$ (P-value)

c Control

0 h | 3 h
Laser damage
CV zone | PV zone
LysM-GFP SHG

Resident mac-depleted

0 h | 3 h
PV zone
Laser damage
CV zone
LysM-GFP SHG

d Control | Resident mac-depleted

Accumulation score
PV | CV
$P = 0.0002$
$P = 0.7354$
Time post ablation (h)

e Photoactivation-based cell labelling | Isolation of labelled CD45$^+$ cells

CV PV
GFP$^+$ PV zone-derived cells
CV
GFP$^+$ CV zone-derived cells
E-cadherin (PV zone) PA-GFP
FSC / GFP

f PV zone | CV zone

Neutrophil
CX$_3$CR1 MP
MP1 MP2
Monocyte
cDC
pDC
T
B
NK/ILC1
NKT
IFN-γ^{Hi} NKT
tSNE2 / tSNE1

Cell bias towards CV ← | → Cell bias towards PV
MP1
MP2
Neutrophil
NKT
IFN-γ^{Hi} NKT
CX$_3$CR1 MP
Monocyte
pDC
cDC
T
B
NK/ILC1
Ratio (PV/CV)

g *Clec4f* Kupffer cells (MP1 + MP2)

Marco MP2

tSNE2 / tSNE1
Low — High
Scaled expression

h Scaled expression

Il10 MP1 / MP2 * $P = 5.35 \times 10^{-19}$
Il1rn MP1 / MP2 * $P = 1.15 \times 10^{-9}$
Tgfb1 MP1 / MP2 * $P = 9.20 \times 10^{-8}$

i Marco F4/80 E-cadherin

PV/CV Ratio
$P < 0.0001$
PV
CV
Marco$^-$ (MP1) | Marco$^+$ (MP2)

a

Il10

* *P* = 3.19 x 10^{-111}

Scaled expression

MP1 **MP2** CX₃CR1 MP Monocyte cDC pDC Neutrophil NK/ILC1 T NKT IFN-γ^{Hi} NKT B

b

Il10

P = 0.0028

P = 0.0021

Relative expression (*Gapdh*)

MP2 LSEC HSC Hepatocyte

c

Isotype IgG (Control)

0 h — 3 h

CV zone
Laser damage
PV zone
LysM-GFP SHG

Anti-IL-10R antibody (αIL-10R)

0 h — 3 h

PV zone
Laser damage
CV zone
LysM-GFP SHG

P = 0.0260

Ratio (PV/CV)

PV
CV

Control αIL-10R

d

Marco^{+/+}

0 h — 3 h

Laser damage
CV zone
PV zone
LysM-GFP SHG

Marco^{-/-}

0 h — 3 h

Laser damage
CV zone
PV zone
LysM-GFP SHG

P = 0.0136

Ratio (PV/CV)

PV
CV

Marco^{+/+} *Marco^{-/-}*

Figure 2

a

SPF | GF | ABX | *Myd88*⁻/⁻ (SPF)

Marco F4/80 E-cadherin

b

P = 0.0014
P = 0.0132
P = 0.0871

Number of Kupffer cells

757 | 722 | 705 | 836

SPF | GF | ABX | *Myd88*⁻/⁻

c

P = 0.0005
P < 0.0001
P = 0.0005

% Marco⁺ in Kupffer cells

SPF | GF | ABX | *Myd88*⁻/⁻

d

Il10
(Kupffer cells)

P = 0.0115

Relative expression (*Gapdh*)

SPF | ABX

e

Il10
(Tissue lysates)

P = 0.0115

Relative expression (*Gapdh*)

SPF | ABX

f

SPF (Control) | ABX

0 h | 3 h | 0 h | 3 h

Laser damage

CV zone | PV zone | CV zone | PV zone | Laser damage

LysM-GFP SHG | LysM-GFP SHG

P = 0.0001

Ratio (PV/CV)

PV
CV

SPF | ABX

Figure 3

Figure 4

a

1% DSS water | Normal water

Day 0 7 14 21 28 35 39

Gut — Translocation — Liver

PV CV

Portal vein

Gut commensal-driven liver inflammation

b

Fold change (vs healthy *Marco*$^{+/+}$)

1 — 2 4 6 8 10 12 — 14

		Macrophage	Monocyte	Neutrophil	DC	CXCR6$^+$ NK	B	CD8T	NKT	Th17
Healthy	*Marco*$^{+/+}$									
DSS	*Marco*$^{+/+}$									
	Marco$^{-/-}$									

c

CD45$^+$ cells — $P = 0.0512$
x10^4 cells per g tissue
Marco$^{+/+}$ *Marco*$^{-/-}$

Neutrophil — $P = 0.0374$
Marco$^{+/+}$ *Marco*$^{-/-}$

Th17 — $P = 0.0343$
Marco$^{+/+}$ *Marco*$^{-/-}$

d

Marco$^{+/+}$ — *Marco*$^{-/-}$

CV, PV

LysM-GFP SHG

e

ALT — $P = 0.0007$
U/L
Marco$^{+/+}$ *Marco*$^{-/-}$

AST — $P = 0.0057$
Marco$^{+/+}$ *Marco*$^{-/-}$

f

Timp1 — $P = 0.0337$
Relative expression (*Gapdh*)
Marco *Marco*

Col1a1 — $P = 0.0103$
Marco *Marco*

g

Marco$^{+/+}$
Marco$^{-/-}$

Type I collagen E-cadherin

PV zones — $P = 0.0407$
MFI of type I collagen
Marco$^{+/+}$ *Marco*$^{-/-}$

h

Human

Control — PSC

MARCO CD68 CK19

i

In visual fields

x10^3 cells of CD68$^+$ cells
1,180 1,305
$P = 0.0205$
Control PSC

% MARCO$^+$ in CD68$^+$ cells
$P < 0.0001$
Control PSC

Periporal regions

% MARCO$^+$ in CD68$^+$ cells
$P < 0.0001$
Control PSC

Figure 5